

The molecular gas in Luminous Infrared Galaxies I. CO lines, extreme physical conditions, and their drivers

Padelis P. Papadopoulos,^{1*} Paul P. van der Werf,² E.M. Xilouris,³ K.G. Isaak,⁴ Yu Gao,⁵ S. Mühle,⁶

¹Max Planck Institute für Radioastronomie, Auf dem Hügel 69, D-53121 Bonn, Germany

²Leiden Observatory, Leiden University, P.O. Box 9513, NL-2300 RA Leiden, The Netherlands

³Institute of Astronomy and Astrophysics, National Observatory of Athens, I.Metaxa & Vas.Pavlou str., GR-15236, Athens, Greece

⁴Research and Scientific Support Department, European Space Agency, Keplerlaan 1, 2200 AG, Noordwijk, The Netherlands

⁵Purple Mountain Observatory, Chinese Academy of Sciences, Nanjing, Jiangsu 210008, China

⁶Argelander-Institut für Astronomie, Auf dem Hügel 71, D-53121 Bonn, Germany

Accepted ... Received ...; in original form ...

ABSTRACT

We report results from a large molecular line survey of Luminous Infrared Galaxies (LIRGs: $L_{\text{IR}} \gtrsim 10^{11} L_{\odot}$) in the local Universe ($z \leq 0.1$), conducted during the last decade with the James Clerk Maxwell Telescope (JCMT) and the IRAM 30-m telescope. This work presents the CO and ^{13}CO line data for 36 galaxies, further augmented by multi-J total CO line luminosities available for other IR-bright galaxies from the literature. This yields a combined sample of $N=70$ galaxies with the star-formation (SF) powered fraction of their IR luminosities spanning $L_{\text{IR}}^{(*)} \sim (10^{10} - 2 \times 10^{12}) L_{\odot}$, and a wide range of morphologies. Simple comparisons of their available CO Spectral Line Energy Distributions (SLEDs) with local ones, as well as radiative transfer models discern a surprisingly wide range of average ISM conditions, with most of the surprises found in the high-excitation regime. These take the form of global CO SLEDs dominated by a very warm ($T_{\text{kin}} \gtrsim 100$ K) and dense ($n \gtrsim 10^4 \text{ cm}^{-3}$) gas phase, involving galaxy-sized ($\sim (\text{few}) \times 10^9 M_{\odot}$) gas mass reservoirs under conditions that are typically found only for $\sim (1-3)\%$ of mass per typical SF molecular cloud in the Galaxy. Furthermore some of the highest excitation CO SLEDs are found in Ultra Luminous Infrared Galaxies (ULIRGs, $L_{\text{IR}} \geq 10^{12} L_{\odot}$), and surpass even those found solely in compact (star-formation)-powered hot-spots in Galactic molecular clouds. Strong supersonic turbulence and high cosmic ray (CR) energy densities rather than far-UV/optical photons or SNR-induced shocks from individual SF sites can globally warm the large amounts of dense gas found in these merger-driven starbursts and easily power their extraordinary CO line excitation. This exciting possibility can now be systematically investigated with Herschel and ALMA. As expected for an IR-selected (and thus (SF rate)-selected) galaxy sample, only few “cold” CO SLEDs are found, and for fewer still a cold low/moderate-density and gravitationally bound state (i.e. Galactic-type) emerges as the most likely one. The rest remain compatible with a warm and gravitationally unbound low-density phase often found in ULIRGs. Such degeneracies, prominent when only the low-J SLED segment ($J=1-0, 2-1, 3-2$) is available, advise against using its CO line ratios and the so-called $X_{\text{CO}} = M(\text{H}_2)/L_{\text{CO}}(1-0)$ factor as star-formation mode indicators, a practice that may have lead to misclassification of the ISM environments of IR-selected gas-rich disks in the distant Universe. Finally we expect that the wide range of ISM conditions found among LIRGs will strongly impact the X_{CO} factor, an issue we examine in detail in paper II (Papadopoulos et al. 2012).

Key words: galaxies: ISM – galaxies: starburst – galaxies: AGN – galaxies: infrared – ISM: molecules – ISM: CO

1 INTRODUCTION

The population of luminous infrared galaxies (LIRGs), discovered by the *Infrared Astronomical Satellite (IRAS)* to have bolometric

* Email: padelis@mpifr-bonn.mpg.de

luminosities dominated by the infrared part of their Spectral Energy Distributions (SEDs) (e.g. Soifer et al. 1987), contains some of the most extreme star-forming systems in the local Universe. At $L_{\text{IR}} \gtrsim 10^{11} L_{\odot}$ these deeply dust enshrouded star-forming systems dominate the luminosity function of the local Universe, and at $L_{\text{IR}} \geq 10^{12} L_{\odot}$ surpass even optically selected QSOs (Soifer & Neugebauer 1991; Sanders & Ishida 2004 and references therein). Their large reservoirs of molecular gas mass ($\sim 10^9$ - $10^{10} M_{\odot}$) discovered via CO J=1-0 observations (Tinney et al. 1990; Sanders, Scoville, & Soifer 1991; Solomon et al. 1997), along with clear evidence of strong dynamical interactions and mergers in many LIRGs (e.g. Sanders & Ishida 2004), make these systems unique local examples of dust-enshrouded galaxy formation in the distant Universe (e.g. Smail, Ivison, & Blain 1997; Hughes et al. 1998).

Interferometric imaging of the CO 1-0 line (and occasionally of J=2-1), revealed gas disks with $D \lesssim 0.5$ kpc and surface densities $\Sigma(\text{H}_2) \sim (10^2$ - $10^4) M_{\odot} \text{pc}^{-2}$, often decoupled from the stellar components of merging galaxies (e.g. Sanders et al. 1988a; Wang et al. 1991; Planesas et al. 1991; Bryant & Scoville 1996, 1999; Downes & Solomon 1998). Naturally the CO(2-1)/(1-0) ratio was the first to be systematically measured (Krügel et al. 1990; Braine & Combes 1992; Horellou et al 1995; Aalto et al. 1995; Albrecht, Krügel, & Chini 2007) even if it is insensitive to the presence of dense and warm gas typical near SF sites. The advent of submm interferometric CO(3-2) imaging revealed the distributions of such gas in LIRGs via the distribution of CO (3-2)/(1-0), (3-2)/(2-1) ratios (e.g. Sakamoto et al. 2008; Wilson et al. 2009; Iono et al. 2007, 2009), but its utility remains limited by dissimilar u-v coverage and lack of zero-spacing information (Iono et al. 2004). Thus single dish measurements of total molecular line luminosities and their ratios remain a primary tool for probing the average molecular gas properties in LIRGs (and a prerequisite for interferometric images that contain all spatial information).

Ideally a combination of low to mid-J rotational lines of heavy rotor molecules with high critical densities such as HCN ($n_{\text{cr}} \sim (2$ - $40) \times 10^5 \text{cm}^{-3}$ for J=1-0, 3-2), and CO J+1→J lines from J=0, 1, up to at least $J \geq 2$ ($E_3/k_B \sim 33$ K, $n_{\text{crit}} \sim 10^4 \text{cm}^{-3}$) are necessary to probe the large range of physical properties within GMCs ($T_{\text{kin}} \sim (15$ - $100)$ K, $n(\text{H}_2) \sim (\text{few}) \times (10^2$ - $10^6) \text{cm}^{-3}$). Sensitivity limitations and/or lack of multi-beam receivers confined such measurements to few nearby LIRGs and mostly towards their nuclei (e.g. Devereux et al. 1994; Dumke et al. 2001; Meier et al. 2001; Zhu et al. 2003), while heavy rotor molecular lines are faint with $\text{HCN}(1-0) \sim (1/5$ - $1/10) \times \text{CO}(1-0)$ even in ULIRGs, and as low as $\sim 1/40 \times \text{CO}(1-0)$ in typical spirals (Solomon et al. 1992). Multi-J observations of the luminous CO line emission are not limited by sensitivity rather by the lack of multi-beam receivers and/or beam-matched observations in widely different frequencies. Thus, while several studies use CO(3-2)/(1-0) as a warm/dense gas tracer in substantial LIRG samples (e.g. Mauersberger et al. 1999; Yao et al. 2003; Narayanan 2005; Mao et al. 2011), these are typically confined solely within their nuclear regions. CO J=4-3 or higher-J line observations are even more sporadic, hindered by increasing atmospheric absorptions at $\nu \gtrsim 460$ GHz, while also confined to the nuclear regions of nearby LIRGs (e.g. White et al. 1994; Güsten et al. 1996; Petitpas & Wilson 1998; Nieten et al. 1999; Mao et al. 2000; Bayet et al. 2006). This is unfortunate since, while the difficulty of measuring reliable CO line ratios increases with wider J-level separations (for the same dish: $\Omega_{J+1 \rightarrow J}^{(\text{beam})} / \Omega_{1 \rightarrow 0}^{(\text{beam})} = (J+1)^{-2}$), so does their diagnostic power. Nevertheless molecular Spectral Line Energy Distributions (SLEDs) remain the key tool for probing the average state of the molecular gas in galaxies, and for estimating to-

tal and star-forming molecular gas masses. Finally local CO SLEDs provide a necessary benchmark for the usually more sparsely sampled ones for galaxies at high redshifts (e.g. Weiss et al 2007), and have been recently used as SF mode (merger versus disk-driven star formation) indicators for gas-rich near-IR selected disks in the distant Universe (Dannerbauer et al. 2009; Daddi et al. 2010).

We used the James Clerk Maxwell Telescope (JCMT¹) on Mauna Kea in Hawaii (USA), and the IRAM 30-meter telescope at Pico Veleta (Spain) to conduct a multi-J CO, HCN line survey of such systems and study the molecular ISM in some of the most extreme star-forming systems in the local Universe. First results regarding the CO J=6-5 lines and dust emission SEDs have already been published (Papadopoulos et al. 2010a,b, hereafter P10a,b). In this paper we present the entire (JCMT)+(IRAM) CO, ¹³CO line dataset, further augmented with all reliable measurements of *total* CO line luminosities of LIRGs from the literature, which yields currently the largest such database assembled for local star-forming galaxies. For a few LIRGs in our sample their CO SLEDs have been extended towards higher-J levels (from J=5-4 up to J=13-12) with the SPIRE/FTS aboard the Herschel Space Observatory.

The layout of this work is as follows: in Sections 2, 3 we describe the sample and the observations, Section 4 contains the data reduction, the literature search, and line flux rectifications for any discrepant values found. In Section 5 we investigate the molecular ISM excitation in LIRGs using comparisons with local environments, and propose a new two-phase ISM model for extreme starbursts, motivated by recent views on SF-powered radiative feedback onto the ISM. In the same section we also briefly discuss the role of AGN in driving the global ISM excitation. In section 6 one-phase radiative transfer modeling of the CO line ratios is used to systematically extract the average densities, temperatures, and dynamical states of the average ISM environments encountered in our sample, and assemble a comprehensive picture of their range. In section 7 we present the CO SLED excitation range possible from J=1-0 up to J=7-6, and discuss their power sources. There we also discuss the (CO SLED)↔(ISM state) degeneracies, and their impact on the classification of SF modes in galaxies, using the CO line ratios of recently discovered near-IR selected gas-rich disks at high redshifts as an example. We present our conclusions in Section 8, where we also list a few important questions regarding the expected effects of ISM excitation conditions on molecular gas mass estimates in LIRGs and ULIRGs, the subject of our second paper (Papadopoulos et al. 2012). Throughout this work we adopt a flat Λ -dominated cosmology with $H_0 = 71 \text{ km s}^{-1} \text{ Mpc}^{-1}$ and $\Omega_m = 0.27$.

2 THE SAMPLE

The sample was drawn from two CO J=1-0 surveys of LIRGs by Sanders et al. 1991, and Solomon et al. 1997 (themselves drawn from the *IRAS* BGS flux-limited sample with $f_{60 \mu\text{m}} > 5.24 \text{ Jy}$; Soifer et al. 1987, 1989; Sanders et al. 2003), so that all galaxies in our sample have at least one measurement of this basic H₂-tracing line. We imposed two additional criteria, namely: a) $z \leq 0.1$ (the maximum redshift for which the JCMT B-band receivers can tune to CO J=3-2), and b) compact CO-emitting regions (sizes from CO interferometric images) so that single telescope pointings or

¹ The James Clerk Maxwell Telescope is operated by the Joint Astronomy Centre (JAC) on behalf of the Science and Technology Facilities Council (STFC) of the United Kingdom, the Netherlands Organisation for Scientific Research, and the National Research Council of Canada

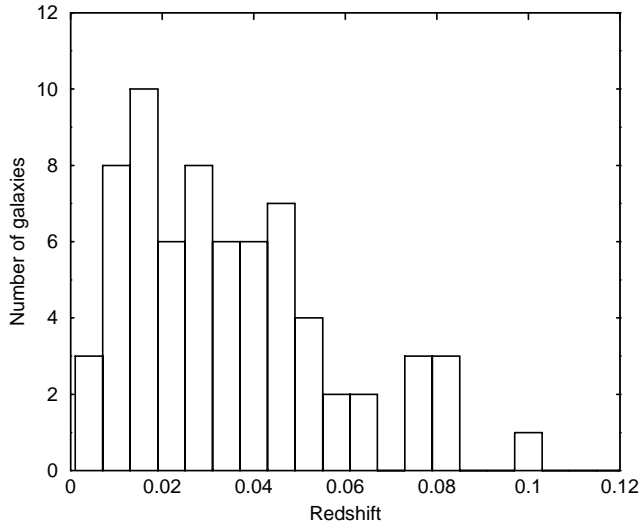


Figure 1. The redshift distribution of the combined sample (see section 2).

small maps can record total line fluxes. If CO images were unavailable then radio continuum (Condon et al. 1990, 1996; Crawford et al. 1996), sub-mm dust emission (Lisenfeld, Isaak, & Hills 2000; Mortier et al. 2011) or near-IR images (Zenner & Lenzen 1993; Murphy et al. 1996; Scoville et al. 2000) helped place an upper limit on the size of their CO-bright emission unaffected by extinction. This is because sub-mm emission, sensitive to both the warm dust associated with molecular gas and the cold dust concomitant with the more extended HI (Thomas et al. 2001) sets $\theta_{\text{sub-mm}} > \theta_{\text{CO}}$, while the radio continuum, tied to the far-IR emission through a well-known correlation, traces the star forming regions of LIRGs (Condon et al. 1990) where most of the molecular gas lies.

We have also extensively searched the literature for all local LIRGs whose total CO J+1→J fluxes from J+1=1 up to J+1=3 are measured (for higher-J lines such measurements are currently non-existent in the local Universe). Unfortunately this forced the omission of many, often beam-matched, observations (e.g. Devereux et al. 1994; Mauersberger et al. 1999; Mao et al. 2011) as in many such cases CO line emission extends well beyond the nuclear region where such observations were conducted. The combined sample of 70 LIRGs (Table 3) is currently the largest for which their molecular gas can be studied using CO lines which can probe physical conditions from the quiescent to the star forming phase. Its redshift distribution is shown in Figure 1, while its IR luminosity (the SF-powered part) range is $L_{\text{IR}}^{(*)} \sim (10^{10} - 2 \times 10^{12}) L_{\odot}$ (computed over $\lambda = (8-1000) \mu\text{m}$). The sample is sparse towards low IR luminosities since galaxies with $L_{\text{IR}} \sim (1-5) \times 10^{10} L_{\odot}$ are usually extended (e.g. Tinney et al. 1990) and thus rarely have total CO J+1→J fluxes available for J+1≥3. We tried to alleviate this bias by including the few low- L_{IR} galaxies whose total CO J=1→0, 3→2 line luminosities have been recently measured (Leech et al. 2010).

3 THE OBSERVATIONS

We used the A 3 receiver (211-276 GHz, DSB operation) on the 15-meter JCMT on Mauna Kea in Hawaii (USA), to observe the CO J=2→1 (230.538 GHz), and ^{13}CO J=2→1 (220.398 GHz) lines, and its B 3 (315-370 GHz) and W/C (430-510 GHz) receivers operating in single sideband (SSB) for CO J=3→2 (345.796 GHz) and J=4→3

(461.041 GHz) line observations in our sample. The observations were conducted during several periods from 1999 up to 2010 (see Table 1 for specific periods and typical system temperatures). CO J=3→2 observations beyond 2008 utilized the new 16-beam HARP-B SSB receiver (325-375 GHz). The decommissioning of the W/C JCMT receiver before completion of the survey as well as the several CO J=4→3 lines redshifted into the deep 450 GHz atmospheric absorption band meant that such measurements could be conducted for only 10 out of the original sample of 30 LIRGs.

The Digital Autocorrelation Spectrometer (DAS) was used in all JCMT observations until 2006, while the new spectrometer ACSIS was employed afterwards. At 345 GHz we used its 920 MHz ($\sim 800 \text{ km s}^{-1}$) or 1.8 GHz ($\sim 1565 \text{ km s}^{-1}$) bandwidth mode, depending on the expected line width and the need for maximum sensitivity (i.e. when 920 MHz bandwidth was sufficient to cover the line, dual-channel operation was possible with B 3, and was used for better sensitivity). For the high frequency W/C observations the widest 1.8 GHz bandwidth was used throughout whose $\sim 1170 \text{ km s}^{-1}$ velocity coverage adequately covered the FWZI of all the CO 4→3 lines observed. For the CO, ^{13}CO J=2→1 lines both bandwidth modes were used, yielding $\sim (1200-2345) \text{ km s}^{-1}$ velocity coverage. Beam-switching with frequencies of $\nu_{\text{chop}} = (1-2) \text{ Hz}$, at throws of $120''-180''$ (in azimuth) ensured flat baselines. The beam sizes were: $\Theta_{\text{HPBW}}(230 \text{ GHz}) = 22''$, $\Theta_{\text{HPBW}}(345 \text{ GHz}) = 14''$ and $\Theta_{\text{HPBW}}(461 \text{ GHz}) = 11''$. We checked and updated the pointing model offsets every hour using continuum and spectral line observations of strong sources, with average residual pointing rms scatter $\sigma_r = \sqrt{\sigma_{\text{cl}}^2 + \sigma_{\text{az}}^2} \lesssim 2.5''$.

3.1 The CO J=6→5 observations

The first measurements of the CO J=6→5 line (691.473 GHz) were conducted for the luminous ULIRG/QSO Mrk 231 and the LIRG Arp 193 in our sample using the old JCMT W/D band (620-710 GHz) receiver (operating in SSB mode) on 20 of February and 22 of April 2005 respectively, under excellent, dry conditions ($\tau_{220 \text{ GHz}} \lesssim 0.035$). The typical system temperatures were $T_{\text{sys}} \sim (3700-5500) \text{ K}$ (including atmospheric absorption). The DAS spectrometer was used in its widest mode of 1.8 GHz ($\sim 780 \text{ km s}^{-1}$ at 690 GHz), and beam switching at frequencies of $\nu_{\text{chop}} = 2 \text{ Hz}$ with azimuthal throws of $60''$ resulted in flat baselines. The beam size at 691 GHz was $\Theta_{\text{HPBW}} = 8''$. Good pointing with such narrow beams is crucial and was checked every (45-60) mins using differential pointing with the B3 receiver (350 GHz). This allows access to many more suitable compact sources in the sky than direct pointing with the W/D receiver at 690 GHz, and was found accurate to within $\sigma_r \sim 2.6''$ (rms) during that observing period.

The other CO J=6→5 measurements were conducted during 2009, with the upgraded W/D receiver equipped with new SIS mixers (effectively the same type installed at the ALMA telescopes in this waveband) which dramatically enhanced its performance. The resulting low receiver temperatures ($T_{\text{rx}} \sim 550 \text{ K}$) allowed very sensitive observations with typical $T_{\text{sys}} \sim (1500-3000) \text{ K}$ (including atmospheric absorption) for $\tau_{220 \text{ GHz}} \sim 0.035-0.06$. Dual channel operation (after the two polarization channels were aligned to within $\lesssim 1''$) further enhanced the W/D band observing capabilities at the JCMT (see Table 1). The ACSIS spectrometer at its widest mode of 1.8 GHz was used, while in a few cases two separate tunings were used to create an effective bandwidth of $\sim 3.2 \text{ GHz}$ ($\sim 1390 \text{ km s}^{-1}$ at 690 GHz) so that it adequately covers (U)LIRG CO lines with FWZI $\sim (800-950) \text{ km s}^{-1}$. Rapid beam

Table 1. JCMT: observing periods, CO lines, typical system temperatures

Year	periods	spectral lines	T _{sys} (K) ^a
1999	06/07–20/07	CO 3–2, 4–3	450-700 (B 3), 1130–2380 (W/C)
2001	10/12–28/12	CO 3–2	380-550 (B 3)
2002	24/02–25/02	CO 3–2	630-690 (B 3)
“	17/04–18/04	CO 3–2	760, 1100-1700 (B 3)
“	17/06–30/06	CO 2–1, 3–2	550 (A 3), 430-650, 900-1200 (B 3)
“	20/11–23/11	CO 4–3	2600-4800, 6000-9300 (W/C) ^b
2003	06/11	CO 3–2	4000-4400 (B 3)
2004	20/01	CO 3–2	530-620 (A 3)
“	02/04–29/05	^{12,13} CO 2–1, CO 3–2	300-450 (A 3), 470-2400 (B 3) ^b
“	13/07–25/08	^{12,13} CO 2–1, CO 3–2	320-510 (A 3), 800-1000 (B 3)
“	28/09–10/11	^{12,13} CO 2–1, CO 3–2	300-600 (A 3), 530-1350 (B 3)
“	18/11	CO 4–3	2450-2800 (W/C)
2005	20/02	CO 6–5	4500-5200 (W/D)
“	17/04-23/04	CO 3–2, 4–3, 6–5	720-1100 (B 3), 1600 (W/C), 3700-5500 (W/D)
“	22/08	¹³ CO 2–1	415-420 (A 3)
“	10/10–28/10	^{12,13} CO 2–1	230-420 (A 3)
“	15/12–31/12	^{12,13} CO 2–1, CO 3–2	330-490 (A 3), 750-980 (B 3)
2006	15/12–18/12	¹³ CO 2–1	250-280 (A 3/ACSIS)
2007	16/12–21/12	¹³ CO 2–1	230-280 (A 3/ACSIS)
“	22/02–24/02	¹³ CO 2–1	310-320 (A 3/ACSIS)
2008	09/05	CO 3–2	1630 (HARP-B/ACSIS)
2009	06/01–07/01	CO 6–5	2600-3200, 7500 (W/D, ACSIS) ^b
“	22/01–25/01	CO 6–5	1700-2600, 9000 (W/D, ACSIS) ^b
“	01/02	CO 6–5	2200-3500 (W/D, ACSIS)
“	27/01	CO 6–5	2000-2900 (W/D, ACSIS)
“	02/03	CO 6–5	1300-1500 (W/D, ACSIS)
“	13/03–15/03	CO 6–5	1900-3100 (W/D, ACSIS)
2010	11/09	CO 6–5	1400-1800 (W/D, ACSIS)

^aT_{sys} values include atmospheric absorption. High values of T_{sys}(B 3) > 600 K and T_{sys}(A 3) > 350 K are measured in a few cases close to tuning range limits ($\nu_{\text{sky}} < 320$ GHz for B 3, $\nu_{\text{sky}} < 215$ GHz for A 3), or when $|\nu_{\text{sky}} - 325 \text{ GHz}| < 5 \text{ GHz}$, i.e. close to a strong atmospheric absorption feature at 325 GHz.

^bThe high T_{sys} values found only for VII Zw 31, a circumpolar source at the JCMT latitude, observed at elevation of $\sim 30^\circ$

Table 2. Point source S_ν/T (Jy/K) conversion factors and HPBW values used for the observations and literature data

Telescope ^a	110–115 GHz ^b	210–230 GHz	315–345 GHz ^b	430–461 GHz ^b	620–710 GHz ^b
IRAM 30-m (S _ν /T _A [*])	6.3 ^c (22'')	7.9, 8.7(11'')			
JCMT (S _ν /T _A [*])		25-28(22'')	28-38(14'')	50-74(11'')	49-62(8'')
NRAO 12-m (S _ν /T _R [*])	35 ^d (55'')	55(32'')			
FCRAO 14-m (S _ν /T _A [*])	42(45'') ^e				
Onsala 20-m (S _ν /T _A [*])	31(33'')				
SEST (S _ν /T _{mb})	27(45'') ^f	41(22'') ^f			
HHSMT (S _ν /T _{mb})			50 ^g (23'')		
NRO 45-m (S _ν /T _{mb})	2.4 ^h (14.5'')				
CSO (S _ν /T _{mb})			43 ⁱ (21'')		

^aThe telescope and temperature scale type (see Kutner & Ulich 1981 for definitions).

^bThe frequency range per receiver.

^cFor T_A^{*} = (B_{eff}/F_{eff}) × T_{mb} = 0.789 × T_{mb}: S_ν/T_{mb} = 4.95 Jy/K, used to obtain the CO 1-0 fluxes from all the IRAM 30-m spectra in the literature that are reported in the T_{mb} scale (unless a different S_ν/T_{mb} is mentioned).

^dMeasured at 110 GHz (section 2.3.2), also in the NRAO 12-m User's Manual 1990 Edition, Figure 14.

^eThe T_R^{*} scale is sometimes used to report data from the FCRAO 14-m (e.g. Sanders et al. 1986), for which S_ν/T_R^{*} = η_{fss} (S_ν/T_A^{*}) = 31.5 (Jy/K) (for η_{fss} = 0.75) is adopted.

^f<http://www.lis.eso.org/lasilla/Telescopes/SEST/html/telescopeinstruments/telescope/index.html>.

^gThe Heinrich Hertz Submillimeter Telescope (Arizona, USA) (from Narayanan et al. 2005).

^hFor the NRO 45-m telescope in Nobeyama (Japan) at 115 GHz: $\Gamma = (8k_B/\pi D^2)(\eta_{mb}/\eta_a)$ and adopting $\eta_a = 0.32$, $\eta_{mb} = 0.44$ (from the NRO website).

ⁱCaltech Submillimeter Observatory (CSO): $\Gamma = (8k_B/\pi D^2)(\eta_{mb}/\eta_a)$, where $D = 10.4 \text{ m}$, $\eta_{mb} = 0.746$ and $\theta_{1/2} = 1.22(\lambda/D)$ yielding $\eta_a/\eta_{mb} = 0.76$ (using $\Omega_A A_e = \lambda^2$ and $\eta_a = A_e/A_g$, $\eta_{mb} = \Omega_{mb}/\Omega_A$).

switching at $\nu_{\text{chop}}=4$ Hz (continuum mode) and azimuthal throw of $30''$ yielded very flat baselines under most circumstances. The pointing model was updated every 45-60 mins using observations of compact sources with the W/D receiver, as well as differential pointing with the A 3 receiver, yielding rms residual error radius of $\sigma_r \sim 2.2''$. The final CO J=6–5 observations were conducted in 2011 during which IZw 1 was observed, with only one W(D) receiver channel functioning, under dry conditions ($\tau_{220 \text{ GHz}} \lesssim 0.05$) that yielded $T_{\text{sys}} \sim (1400-1800)$ K. The same beam-switching scheme was used, while two separate tunings yielded an effective bandwidth of ~ 3.2 GHz covering the wide CO line of this ULIRG/QSO (e.g. Barvainis et al. 1989). The pointing uncertainty remained within the range of previous CO J=6–5 observations. Nevertheless we wish to note that isolated cases of large pointing offsets reducing the observed CO J=6–5 line fluxes have been found (e.g. for Arp 220, see P10a and P10b), and may have affected a few of these highly demanding CO line measurements.

3.2 The IRAM 30-m observations

Observations of CO, ^{13}CO J=1–0, 2–1 with the IRAM 30-m telescope were conducted during two sessions in 2006 namely, June from 20 to 25, and November from 26 to 28. In both periods the A100/B100 (3 mm) and A230/B230 (1 mm) receivers were used, connected to the 1 MHz (A100/B100, 512 MHz) and 4 MHz (A230/B230, 1 GHz) filterbanks. During the first period the A230/B230 receivers were used to observe the ^{12}CO J=2–1 line. If the latter was strong and detected in about a hour or less, the 1 mm receivers were then re-tuned to ^{13}CO J=2–1. For sources with very weak ^{12}CO lines (e.g. 08030+5243, 08572+3915), no attempt of observing ^{13}CO J=2–1 was made. Data were acquired under New Control System (NCS) in series of four-minute scans, each comprised of eight 30-sec subscans. The typical system temperatures (including atmospheric absorption) for the CO 2–1 observations were $T_{\text{sys}}(210-230 \text{ GHz}) \sim (220-500)$ K, with the lowest mostly during the ^{13}CO observations (though for occasional tunings towards the edge of the band and/or bad weather conditions $T_{\text{sys}} \sim (700-900)$ K). For most sources data were acquired in two or more different days to ensure a line detection, and as a consistency check. Pointing and focus were checked frequently during the observations with residual pointing errors $\sigma_r \sim 3''$ (rms).

During the November period receivers A100/B100 were used to observe ^{13}CO J=1–0 line simultaneously to the ^{12}CO J=2–1 line observed with A230/B230 (tuned to the same line each time). The pointing error stayed $\lesssim 3''$ (rms), except during November 26 when it went up to $\sim 6''$ (corresponding data were omitted). The typical system temperatures were $T_{\text{sys}}(110 \text{ GHz}) \sim 110-160$ K, $T_{\text{sys}}(115 \text{ GHz}) \sim (200-380)$ K, and $T_{\text{sys}}(210-230 \text{ GHz}) \sim (330-425)$ K. Finally, in order to maintain very flat baselines, the wobbler switching (nutating subreflector) observing mode with a frequency of 0.5 Hz and beam throws of $180''-240$ was employed during both observing sessions. The beam sizes were: $\Theta_{\text{HPBW}}(110 \text{ GHz})=22''$ and $\Theta_{\text{HPBW}}(210-230 \text{ GHz})=11''$, with corresponding beam efficiencies² of: $B_{\text{eff}}(110 \text{ GHz})=0.75$, $B_{\text{eff}}(230 \text{ GHz})=0.52$ and $B_{\text{eff}}(210 \text{ GHz})=0.57$, and forward beam efficiencies of $F_{\text{eff}}(3 \text{ mm})=0.95$ and $F_{\text{eff}}(1 \text{ mm})=0.91$. We also note that in most cases we had redundant CO J=2–1 measurements with the JCMT, and then: a) adopted the average when JCMT/IRAM values agreed to within 20% (most cases), or b)

adopted the JCMT measurement (as its wider beam is less prone to flux loss due to pointing offsets and/or beam-throw/flux-loss uncertainties) if a discrepancy larger than the aforementioned was found.

4 DATA REDUCTION, LINE INTENSITY ESTIMATES, LITERATURE DATA

In both telescopes the output spectra are in the T_A^* scale (see Kutner, & Ulich 1981). We inspected all individual 10min/(4-6)min JCMT/IRAM spectra for baseline ripples and to clip any intensity “spikes” in individual channels. The edited spectra were then co-added using a $1/\sigma^2$ -weighting scheme and linear baselines were subtracted from each final co-added spectrum. These spectra are shown in Figures 2 and 3 and were used to derive the velocity-integrated molecular line flux densities from

$$\begin{aligned} S_{\text{line}} &= \int_{\Delta V} S_{\nu} dV = \frac{8k_B}{\eta_a^* \pi D^2} K_c(x) \int_{\Delta V} T_A^* dV \\ &= \frac{\Gamma(Jy/K)}{\eta_a^*} K_c(x) \int_{\Delta V} T_A^* dV, \end{aligned} \quad (1)$$

where $\Gamma_{\text{JCMT}}=15.62$, $\Gamma_{\text{IRAM}}=3.905$ and η_a^* is the aperture efficiency defined against the T_A^* scale ($\eta_a^* = \eta_a / \eta_{\text{rss}}$, where η_a is the aperture efficiency measured against the T_A' scale, as is more typical, and η_{rss} is the rearward spillover and scattering efficiency, Rohlfs & Wilson (1996), Eqs 8.16, 8.17). The factor $K_c(x) = x^2 / (1 - e^{-x^2})$, with $x = \theta_s / (1.2 \theta_{\text{HPBW}})$ and θ_s = source diameter, accounts for the geometric coupling of the beam (its gaussian part) to a disk-like source, when a CO emission size was available, and $2\sigma_r \lesssim \theta_s \lesssim \theta_{\text{HPBW}}$ where σ_r is the pointing error radius (see 4.1). The total point-source conversion factors S_{ν}/T adopted for the JCMT, the IRAM 30-m telescope, and all the data gleaned from the literature (for the corresponding output antenna temperature scales) are comprehensively tabulated in Table 2.

4.1 Aperture efficiencies, line intensity uncertainties, biases

Aperture efficiencies of large high-frequency sub-mm telescopes such as the JCMT can change significantly (especially for $\nu \gtrsim 460$ GHz) depending on a variety of factors (e.g., elevation, thermal relaxation of the dish or its re-shaping after an holography session). In order to track them over an decade of observations (during which the JCMT dish has been re-adjusted quite a few times) we conducted frequent aperture efficiency measurements using planets and adopted the average η_a^* obtained per observing period for deriving the line fluxes of all the sources observed during it. In many cases, as a cross-check, we distributed the measurements of very CO-luminous LIRGs over several widely separated periods, during which very different aperture efficiencies (sometimes up to a factor of ~ 2) were often measured. In all such cases Equation 1, with the appropriate η_a^* values, yielded velocity-integrated line fluxes in excellent agreement. Indicatively most aperture efficiencies measured for the JCMT lay within $\eta_a^* \sim 0.41-0.56$ (B-band, 315-350 GHz), and $\eta_a^* \sim 0.21-0.31$ (C-band, 430-461 GHz). For the three periods of the more demanding W/D band observations we derived $\eta_a^* = 0.25$ (2005), 0.32 (2009), 0.27 (2010) from planetary measurements. The uncertainties for the reported velocity-integrated line flux densities have been computed from

² <http://www.iram.fr/IRAMES/index.htm>

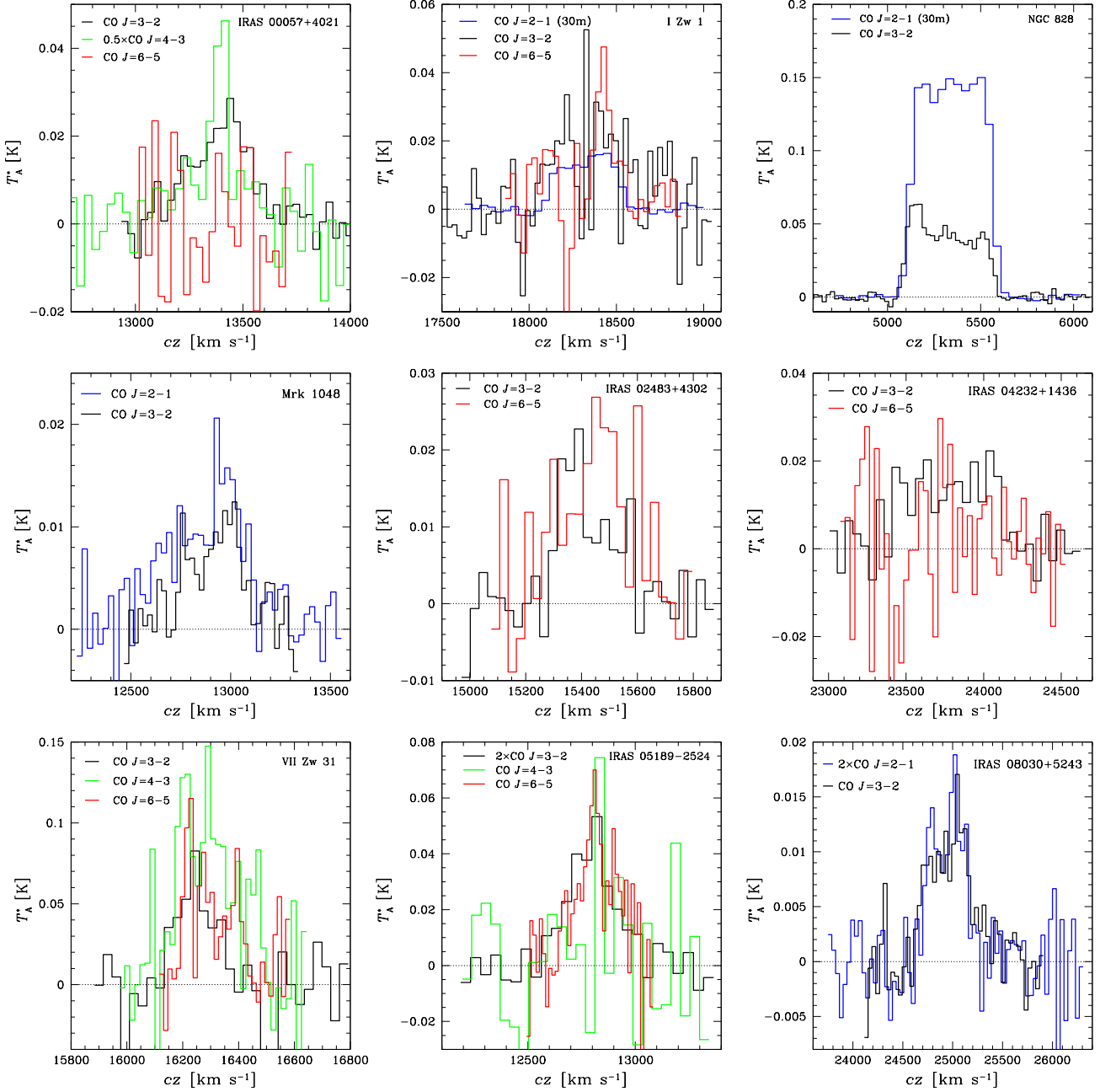


Figure 2. The high- J CO $J+1 \rightarrow J$, $J+1 \geq 3$ spectra. In the few cases where all three CO $J=3-2$, $4-3$ and $6-5$ lines are available we omit the overlay of CO $J=2-1$ in order to reduce confusion (the $J=2-1$ lines are all shown in Figure 3). The velocities are with respect to $V_{\text{opt}} = cz_{\text{CO}}$ (Table 3), and with typical resolutions $\Delta V_{\text{ch}} \sim (10-50) \text{ km s}^{-1}$. A common color designated per transition is used in all frames.

$$\frac{\Delta S_{\text{line}}}{S_{\text{line}}} = \left[\left(\frac{\delta T_{\Delta V}}{T_{\Delta V}} \right)_{\text{th}}^2 + \left(\frac{\delta T_{\Delta V}}{T_{\Delta V}} \right)_{\text{cal}}^2 + \left(\frac{\delta \eta}{\eta} \right)^2 \right]^{1/2}, \quad (2)$$

where $\delta T_{\Delta V}$ is the stochastic error of the average line intensity $T_{\Delta V}$ (averaged over the line FWZI ΔV), η is the telescope efficiency factor (used to derive the integrated line flux from the temperature scale of the output spectrum, e.g., η_a^* for T_A^*)³, and $\delta \eta$ its

uncertainty. The first term is estimated from the spectra shown in Figures 2, 3 using

$$\left(\frac{\delta T_{\Delta V}}{T_{\Delta V}} \right)_{\text{th}} = \frac{\delta T_{\text{chan}}}{T_{\Delta V}} \left(\frac{N_{\Delta V} + N_{\text{bas}}}{N_{\Delta V} N_{\text{bas}}} \right)^{1/2}, \quad (3)$$

where δT_{chan} is the stochastic intensity dispersion, estimated from the line-free part of the spectrum (for a given velocity channel width ΔV_{chan}), while $N_{\Delta V} = \Delta V / \Delta V_{\text{chan}}$ and

³ More precisely the 3rd term in Equation 2 embodies the uncertainty of total efficiency factor $\eta_l \eta_{f_{ss}}$ needed to convert the T_A^* scale (cor-

rected only for atmospheric extinction) to a final fully corrected (apart from source-beam coupling) T_R^* (or T_{mb}) scale.

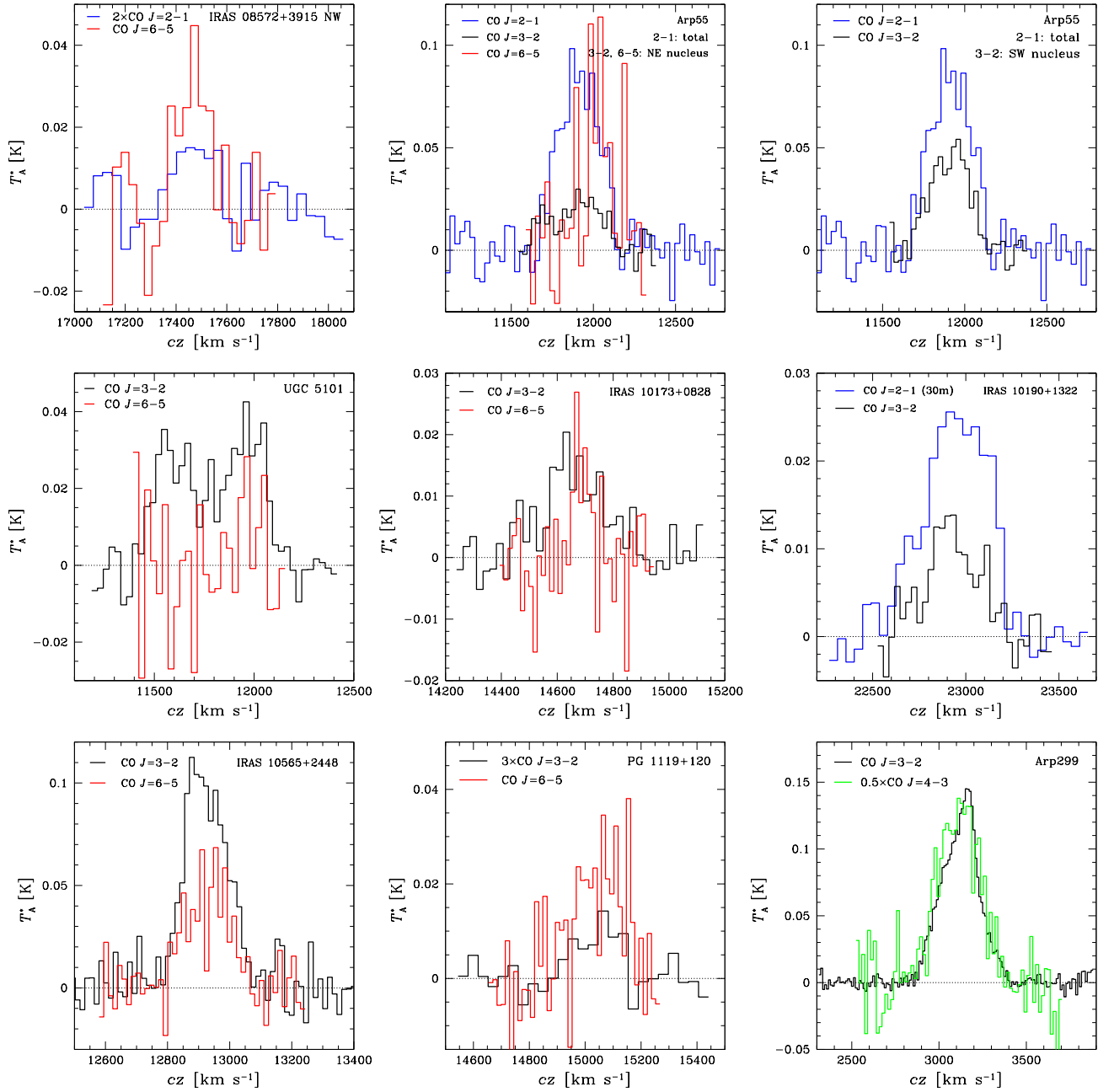


Figure 2 – *continued* The high-J CO $J+1 \rightarrow J$, $J+1 \geq 3$ spectra. In the few cases where all three CO $J=3-2$, $4-3$ and $6-5$ lines are available we omit the overlay of CO $J=2-1$ in order to reduce confusion (the $J=2-1$ lines are all shown in Figure 3). The velocities are with respect to $V_{\text{opt}} = cz_{\text{CO}}$ (LSR) (Table 3), and with typical resolutions $\Delta V_{\text{ch}} \sim (10-50) \text{ km s}^{-1}$. A common color designated per transition is used in all frames.

$N_{\text{bas}} = 2\Delta V_{\text{bas}}/\Delta V_{\text{chan}}$ are the number of channels within the line FWZI and the line-free baseline (with $\Delta V_{\text{bas}}/\Delta V_{\text{chan}}$ channels symmetrically around the line) respectively. The second term in Equation 2 accounts for line calibration errors (due to a host of factors such as imprecise knowledge of the calibration loads, uncertainties in the atmospheric model and the derived extinction etc). Observations of numerous strong spectral line standards and planets during each observing period yielded intensity dispersions of $\sim 15\%$ (230 GHz and 345 GHz), $\sim 20\%$ (460 GHz), and $\sim 25\%$ (690 GHz), which we adopt as the combined calibration (cal) and

$\delta\eta/\eta$ uncertainties per observing band at the JCMT. For the 30-m we consider these to be $\sim 15\%$ for both 3 mm and 1 mm bands.

Finally, even with the accurate tracking and pointing achievable by enclosed telescopes such as the JCMT, the residual rms pointing errors and the narrow beams of large mm/sub-mm telescopes at high frequencies can lead to a substantial and systematic reduction of measured fluxes of compact sources. We try to account for this as described in P10a, by applying a $\langle G \rangle$ scaling factor to the line fluxes of all point-like sources with CO emission region diameters of $\theta_{\text{CO}} \leq 2\sigma_r$ (where $\sigma_r(\text{JCMT}) = 2.5''$ and $\sigma_r(\text{IRAM}) = 3''$ are the pointing error radii). This factor is (see P10a):

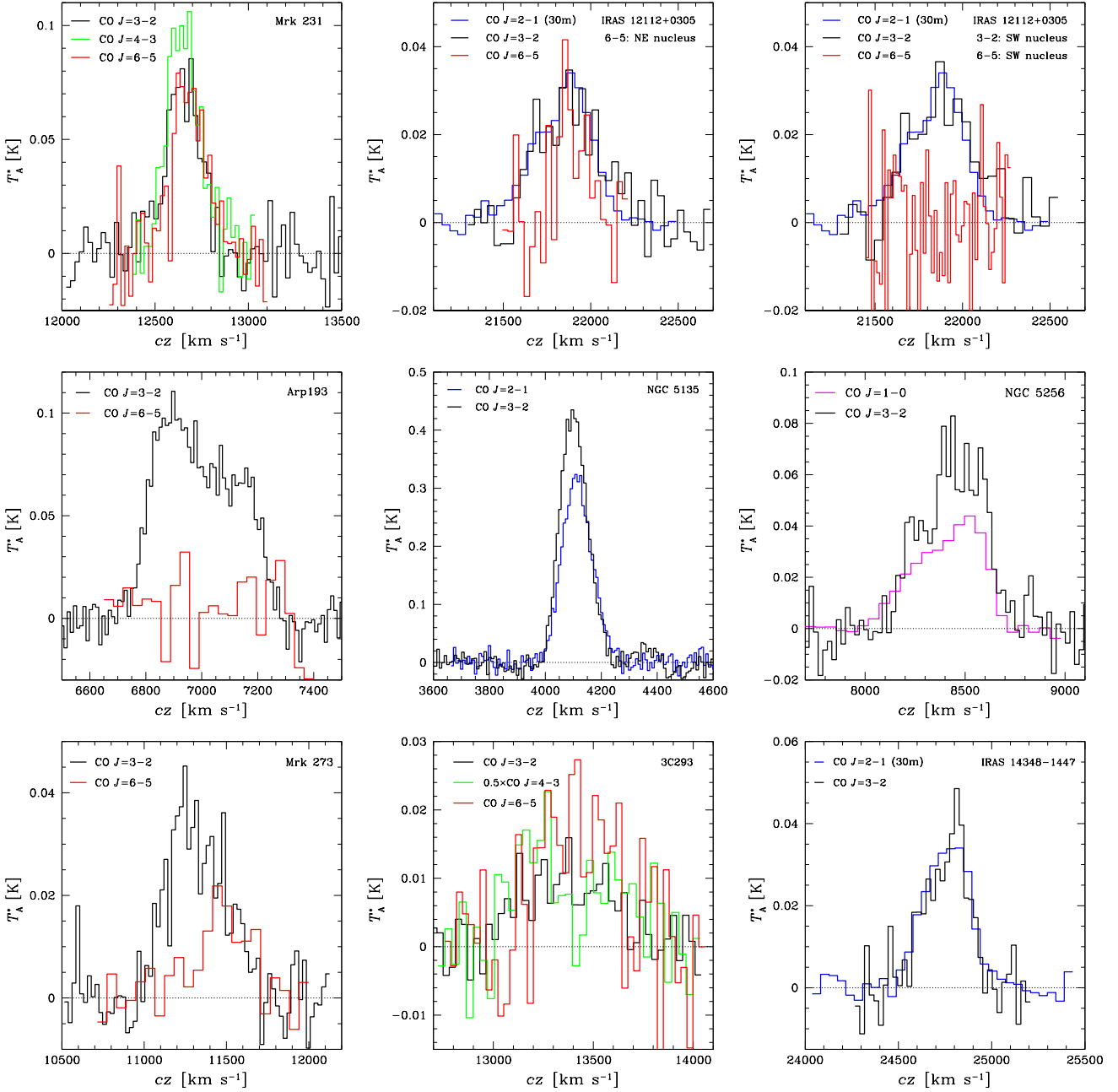


Figure 2 – *continued* The high- J CO $J+1 \rightarrow J$, $J+1 \geq 3$ spectra. In the few cases where all three CO $J=3-2$, $4-3$ and $6-5$ lines are available we omit the overlay of CO $J=2-1$ in order to reduce confusion (the $J=2-1$ lines are all shown in Figure 3). In the case of NGC 5256 only the CO $J=1-0$, $3-2$ lines are available. The velocities are with respect to $V_{\text{opt}} = cz_{\text{CO}}$ (Table 3), and with typical resolutions $\Delta V_{\text{ch}} \sim (10-50) \text{ km s}^{-1}$. A common color designated per transition is used in all frames.

$$G(\sigma_r) = 1 + 8 \ln 2 \left(\frac{\sigma_r}{\sqrt{2} \theta_{1/2}} \right)^2, \quad (4)$$

where $\theta_{1/2}$ is the beam HPBW, $\sigma_r/\sqrt{2}$ is the rms pointing error per pointing coordinate. For $\theta_{\text{CO}} \leq 2\sigma_r$, $K_c(x)$ is replaced in Equation 1 by $G(\sigma_r)$ as the beam-source coupling correction is overtaken by the pointing error correction. At 345 GHz and 460 GHz for the JCMT we obtain $\langle G_{345} \rangle = 1.087$ and $\langle G_{460} \rangle = 1.15$, (with negligible correction at 230 GHz), while for the 30-m $\langle G_{230} \rangle = 1.20$ (and negligible correction at 115 GHz). The CO $J=6-5$ observations with HPBW $\sim 8''$ are those most susceptible to this bias and $\langle G_{690} \rangle$ has

been estimated from the pointing rms *per observing session*, yielding a range $\langle G_{690} \rangle = 1.17-1.37$. For sources with CO (or sub-mm dust emission) sizes of $2\sigma_r \lesssim \theta_s \lesssim \theta_{1/2}$ the K_c factor is used in Equation 1. Finally in the cases where large offsets were found between the presumed CO source center and the observed positions in the literature (see discussion in 4.2) we applied a beam-shift correction factor of $K_{\text{sh}} = \exp [4 \ln 2 (\Delta\theta/\Theta_{\text{HPBW}})^2]$ where $\Delta\theta$ is the (beam center)-source offset (see Table 4).

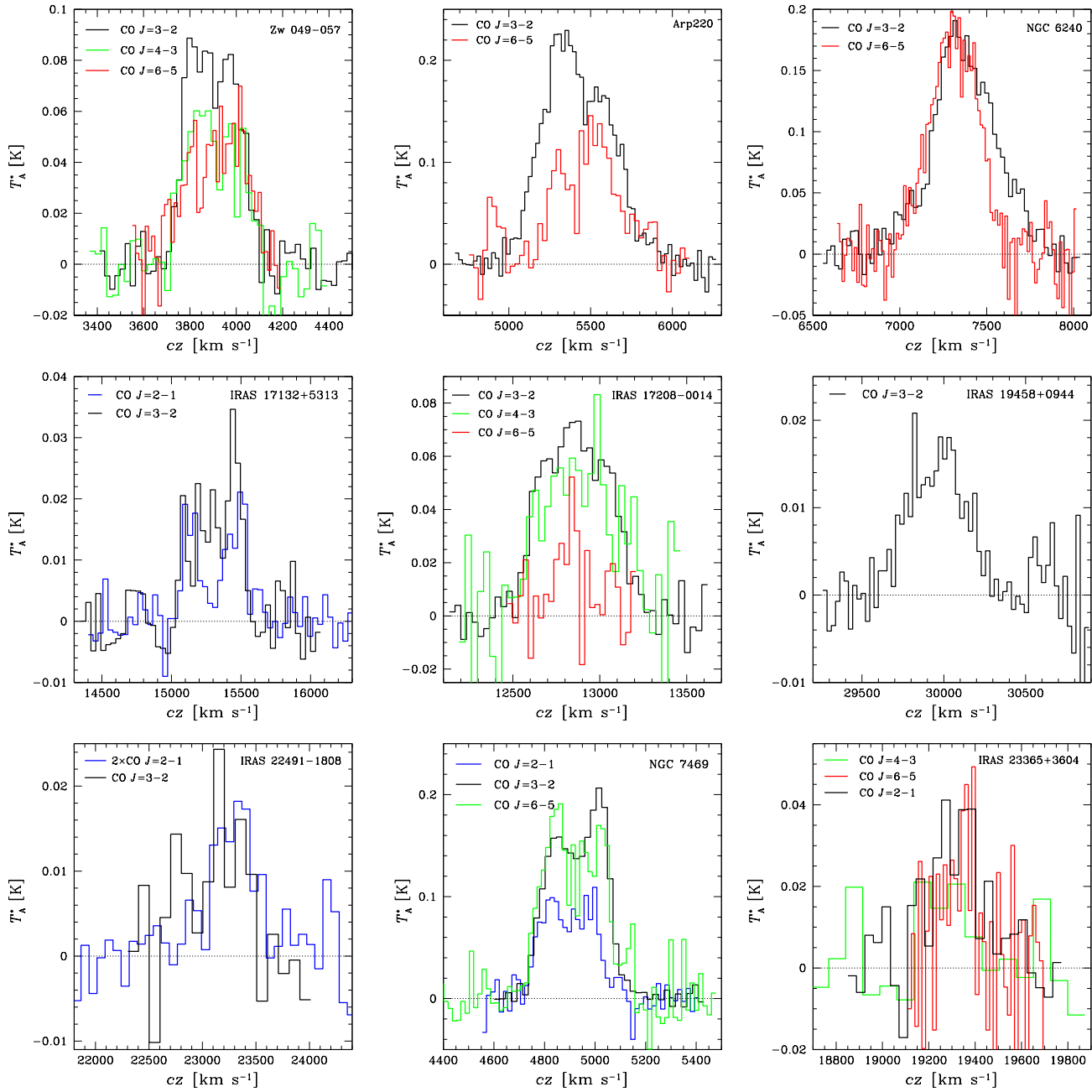


Figure 2 – *continued* The high- J CO $J+1 \rightarrow J$, $J+1 \geq 3$ spectra. In the few cases where all three CO $J=3-2$, $4-3$ and $6-5$ lines are available we omit the overlay of CO $J=2-1$ in order to reduce confusion (the $J=2-1$ lines are all shown in Figure 3). The velocities are with respect to $V_{\text{opt}} = cz_{\text{CO}}$ (LSR) (Table 3), and with typical resolutions $\Delta V_{\text{ch}} \sim (10-50) \text{ km s}^{-1}$. A common color designated per transition is used in all frames.

4.2 Incorporating data from the literature, the final dataset

A detailed literature search for all total CO and ^{13}CO line fluxes available for LIRGs enlarged our sample (see Table 3), while allowing also a consistency check using the duplicate measurements per object (especially for the $J=1-0$ transition). In most cases we find good agreement among the various CO $J=1-0$ fluxes reported in the literature, and between the (much fewer) reported $J=2-1$, $3-2$ line fluxes and our measurements, within the expected uncertainties⁴.

⁴ In the literature the uncertainties of mm/sub-mm line measurements are often underestimated, with only the thermal rms error reported (the first

Most cases of serious discrepancies among CO line fluxes were rectified after accounting for the different source positions often used. This typically occurred because of the positional uncertainties inherent in the optical identification of heavily dust-obscured sources within the large IRAS position error ellipse (e.g. Solomon et al. 1997) and/or the better CO positions obtained for some LIRGs (e.g. via interferometry) and used for subsequent CO observations after the original $J=1-0$ detections with usually large ($\sim 45''-50''$)

term in the expression in Equation 2). In all such cases we assumed a 15% of calibration and η_a uncertainty in addition to the one reported.

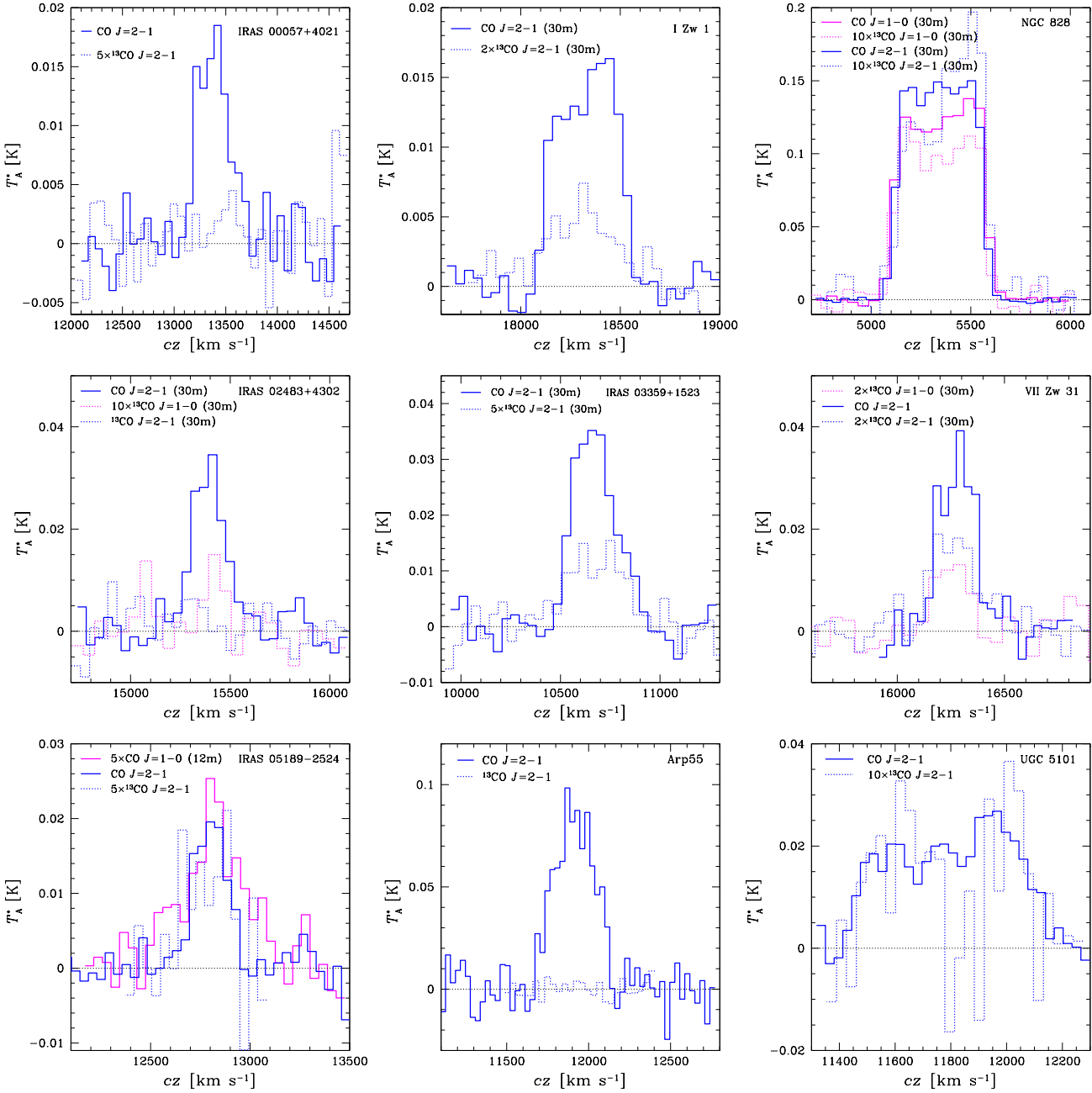


Figure 3. The CO, ^{13}CO line data. The velocities are with respect to $V_{\text{opt}}=cz_{\text{co}}$ (LSR) (Table 3), and with typical resolutions $\Delta V_{\text{ch}} \sim (35\text{--}90) \text{ km s}^{-1}$. A common color designated per transition is used in all frames.

beams were made (e.g. Sanders et al. 1991; Young et al. 1995). Moreover, even when a particular LIRG is optically identified, the multi-component/interacting nature of many such systems can confound the choice of a pointing center for CO single dish observations (e.g. Leech et al. 2010). In the cases where we found different positions used for CO observations reported in the literature, we “shift/scale” the corresponding line fluxes to a common position, the interferometrically-derived CO emission peak of the LIRG (or its near-IR and/or radio continuum peak if the former was unavailable) assuming a source much smaller than the beams used (the case for most LIRGs). This rectified many of the discrepant CO line fluxes, with only a few inconsistent ones remaining, mostly be-

tween new data and much older CO observations (mainly those reported in the Sanders et al. 1991 CO $J=1-0$ survey). These are likely the result of improved calibration techniques (e.g. good sideband rejection), pointing accuracy, and faster beam-switching available for mm/sub-mm telescopes now than in the past.

4.2.1 Resolving a large discrepancy: new CO $J=1-0$ observations of IRAS05189-2524

The largest remaining CO line flux discrepancy is for the LIRG IRAS 05189-2524 with $S_{10}=(91 \pm 18) \text{ Jy km s}^{-1}$ obtained for CO $J=1-0$ with the NRAO 12-m telescope (Sanders et al. 1991) and

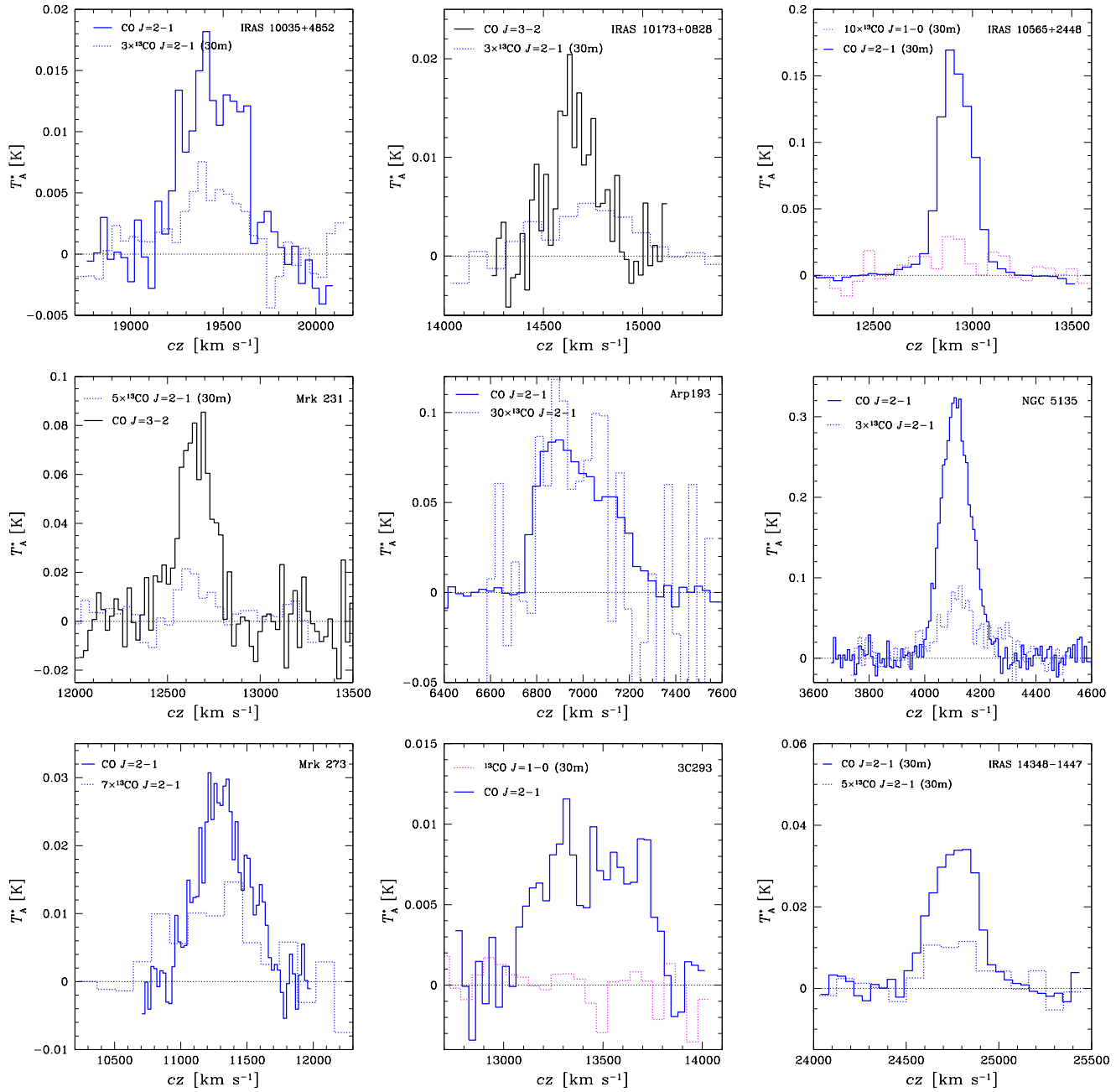


Figure 3 – *continued* The CO, ^{13}CO line data. The velocities are with respect to $V_{\text{opt}}=cz_{\text{co}}(\text{LSR})$ (Table 3), and with typical resolutions $\Delta V_{\text{ch}}\sim(35\text{--}90)\text{ km s}^{-1}$. A common color designated per transition is used in all frames.

$S_{10}=(52 \pm 10)\text{ Jy km s}^{-1}$ with SEST (Strong et al. 2004). The larger value would place this ULIRG to the lowest end of gas excitation of the entire sample, with $r_{32}=0.24$ and $r_{21}=0.32$, typical for the coldest most quiescent GMCs found in the Galaxy and M31 (Loinard et al. 1995; Allen et al. 1995; Fixsen et al. 1999). We used the 12-meter telescope⁵, to re-observe the CO $J=1-0$ line in this ULIRG on the nights of 12, 13 and 24 March, 2008. The final co-added CO $J=1-0$ spectrum (Figure 4) was used to estimate a velocity-integrated line flux of $S_{10}=(43 \pm 8)\text{ Jy km s}^{-1}$, in good

agreement with the value reported by Strong et al. 2004 but less than half that reported by Sanders et al. 1991. We report the average of ours and the Strong et al. 2004 value (Table 4).

⁵ The Kitt Peak 12 m telescope is operated the Arizona Radio Observatory (ARO), Steward Observatory, University of Arizona

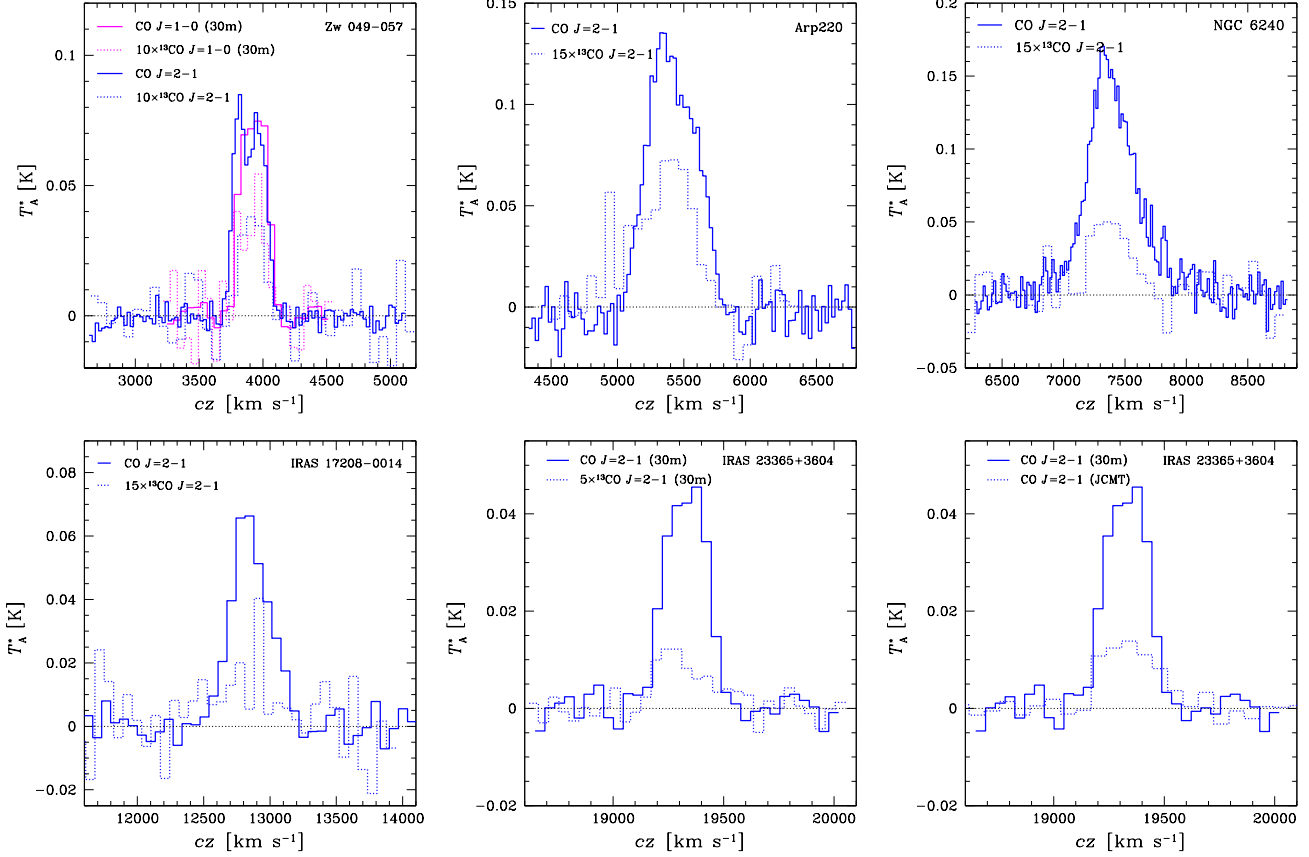


Figure 3 – *continued* The CO, ^{13}CO line data. The velocities are with respect to $V_{\text{opt}}=cz_{\text{CO}}(\text{LSR})$ (Table 3), and with typical resolutions $\Delta V_{\text{ch}}\sim(35\text{--}90)\text{ km s}^{-1}$. A common color designated per transition is used in all frames.

5 THE MOLECULAR GAS IN LIRGS

The ratios of velocity/area-averaged brightness temperatures of CO lines provide the excitation indicators of the average state of the molecular gas, allowing comparisons among LIRGs and well-studied local ISM environments in the Galaxy where individual excitation mechanisms (e.g. SNR shocks, far-UV/IR photons, cosmic rays) can be more easily identified. The luminosity of a line (x) used to compute such brightness temperature line ratios is

$$\begin{aligned} L'_x &= \int_{\Delta V} \int_{A_s} T_{b,x} da dV \\ &= \frac{c^2}{2k_B \nu_{x,\text{rest}}^2} \left(\frac{D_L^2}{1+z} \right) \int_{\Delta V} S_\nu dV, \end{aligned} \quad (5)$$

where $T_{b,x}$ is the rest-frame brightness temperature of the line, ΔV , A_s are the line FWZI and source area, D_L the luminosity distance, and S_ν the line flux density. After substituting astrophysical units

$$L'_x = 3.25 \times 10^3 \left[\frac{D_L^2(\text{Mpc})}{1+z} \right] \left(\frac{\nu_{x,\text{rest}}}{100 \text{ GHz}} \right)^{-2} \left[\frac{\int_{\Delta V} S_\nu dV}{\text{Jy km s}^{-1}} \right], \quad (6)$$

where L'_x is in $\text{K km s}^{-1} \text{ pc}^2$ and $\nu_{x,\text{rest}}$ is the rest frame frequency of line (x). This expression is used to compute the CO line ratios with $r_{J+1,J} = L'_{J+1,J} / L'_J$. The conversion to ordinary luminosity units (L_\odot), used to express the total line luminosities ($L_x = \int L_\nu d\nu$) in CO SLEDs is

$$\begin{aligned} L_x &= \frac{8\pi k_B \nu_{x,\text{rest}}^3}{c^3} L'_x \\ &= 3.18 \times 10^4 \left(\frac{\nu_{x,\text{rest}}}{100 \text{ GHz}} \right)^3 \left[\frac{L'_x}{10^9 L_i} \right] L_\odot. \end{aligned} \quad (7)$$

where $L_i = \text{K km s}^{-1} \text{ pc}^2$.

In Tables 7 and 8 we give the CO line ratios for our sample, and in Figures 5, 6, 7 their frequency distributions. These reveal well-excited lines ($\langle r_{21} \rangle = 0.91$, $\langle r_{32} \rangle = 0.67$) but also a significant excitation range, from low ($r_{21} \sim 0.6\text{--}0.7$, $r_{32} \sim 0.3$) to a high-excitation phase ($r_{21,32} \gtrsim 1$). Luminous CO J=4–3 lines clearly mark the emergence of a second highly excited phase with $r_{43} \gtrsim r_{32}$ and $r_{32} \lesssim r_{21} \lesssim 1$ in several LIRGs (Table 7). This could not happen if the average state was dominated by one phase with optically thick CO lines since then $1 \gtrsim r_{21} \gtrsim r_{32} \gtrsim r_{43} \gtrsim \dots$ (higher-J lines become fainter as subthermal excitation progressively sets in and/or as $E_{J+1,J}/(k_B T_k)$ becomes >1). A high-excitation phase overtaking the lower-excitation one at the transition where the line ratios of the latter fall below unity can indeed reverse this inequality series, provided that this new phase has well-excited and optically thin CO SLEDs. In some cases this occurs already from J=3–2 with $r_{32} \gtrsim r_{21}$ and $r_{21} \lesssim 0.6\text{--}1$ (e.g. IRAS 10190+1322, Arp 220). We note that while the emergence of a second highly-excited phase in global CO and ^{13}CO line emission has been known for some time (e.g. Aalto et al. 1995 and references therein), indications for well-excited and partially optically thin global CO SLEDs are rare.

Table 3. Observational parameters of the combined LIRG sample

Name ^a	RA (J2000) ^b	Dec (J2000) ^b	z (D _L) ^c	($\Delta\theta_\alpha, \Delta\theta_\delta$) ^d	$\langle\theta_s\rangle$ ^e	Refs ^f
00057+4021	00 08 20.58	+40 37 55.5	0.0445 (194.5)	(0'', 0'')	0.81''(co)	1P, ^m
00322-0840* (NGC 157)	00 34 46.48	-08 23 47.8	0.0055 (23.3)	(0'', 0'')	80''(co,sm,x)	2P, ^m
00509+1225 (IZw 1, PG 0050+124)	00 53 34.92	+12 41 35.5	0.0611 (270.3)	(0'', 0'')	$\lesssim 12''$ (co)	3 ^m ,4 ^P
01053-1746* (Arp 236)	01 07 47.00	-17 30 24.0	0.0200 (85.8)	(0'', 0'')	30''(sm,x)	5P, ^{6m}
01077-1707*	01 10 08.20	-16 51 11.0	0.0351 (152.3)	(0'', 0'')	$\lesssim 15''$ (sm)	5P, ^{6m}
01418+1651* (III Zw 35)	01 44 30.50	+17 06 08.0	0.0274 (118.2)	(0'', 0'')	$\lesssim 15''$ (sm)	5P, ^{6m}
02071+3857 (NGC 828, VI Zw 177)	02 10 09.43	+39 11 26.3	0.0178 (76.2)	(0'', 0'')	14''(co)	7P, ^m ,8 ^m
02080+3725* (NGC 834)	02 11 01.55	+37 40 01.3	0.0154 (65.8)	(-2.5'', -2.0'')	13''(cm)	9P, ^{10m}
02114+0456* (Mrk 1027)	02 14 05.60	+05 10 27.7	0.0297 (128.3)	(0'', 0'')	17''(sm,x)	5P, ^{6m}
02321-0900 (NGC 985, Mrk 1048)	02 34 37.74	-08 47 14.7	0.0430 (187.7)	(0'', 0'')	22''(co)	11P, ^m
02401-0013* (NGC 1068)	02 42 40.74	-00 00 47.6	0.0037 (13.3)	(0'', 0'')	40''(co,sm,x)	12P, ^m
02483+4302	02 51 36.01	+43 15 10.8	0.0514 (225.8)	(0'', 0'')	1.75''(co)	1P, ^m
02512+1446* (UGC 2369)	02 54 01.80	+14 58 14.0	0.0312 (135.0)	(0'', 0'')	30''(sm,cm,x)	5P, ^{6m} ,13 ^m
03359+1523	03 38 46.90	+15 32 55.0	0.0353 (153.2)	(0'', 0'')	4.5''(cm)	5P, ^{13m}
04232+1436	04 26 04.94	+14 43 37.9	0.0796 (356.4)	(-1.13'', +0.4'')	$\lesssim 8''$ (cm,sm,x)	14P, ^{6m} ,13 ^m
05083+7936 (VII Zw 031)	05 16 46.51	+79 40 12.5	0.0543 (239.0)	(0'', 0'')	2.3''(co)	1P, ^m
05189-2524	05 21 01.11	-25 21 45.9	0.0427 (186.4)	(+4.0'', +1.0'')	$\lesssim 3''$ (cm,ir)	9P, ^{15m} ,13 ^m
08030+5243	08 06 50.10	+52 35 05.4	0.0835 (375.4)	(0'', 0'')	$\lesssim 0.8''$ (ir)	14P, ^{16m}
08354+2555* (NGC 2623, Arp 243)	08 38 24.10	+25 45 16.5	0.0185 (79.3)	(0'', 0'')	1.65''(co)	17P, ^m
08572+3915 ^g	09 00 25.41	+39 03 54.1	0.0582 (256.9)	(0'', 0'')	$\lesssim 2.1''$ (co)	18P, ^m
09126+4432 (Arp 55)	09 15 54.90	+44 19 54.4	0.0399 (173.3)	(0'', 0'')	1.9'', 1.2''(co,cm,dbl)	5P, 13 ^m , 19 ^m
09320+6134 (UGC 05101)	09 35 51.53	+61 21 11.6	0.0393 (171.1)	(0'', 0'')	1''-2''(ir,co)	14P, ^{15m} ,20 ^m
09586+1600* (NGC 3094)	10 01 26.00	+15 46 14.0	0.0080 (34.0)	(-2.2'', -1.0'')	11''(ir,cm)	21P,22 ^m ,13 ^m
10039-3338* (IC 2545)	10 06 04.50	-33 53 03.0	0.0341 (147.9)	(0'', 0'')	$\lesssim 15''$ (sm)	5P, ^{6m}
10035+4852	10 06 45.83	+48 37 46.1	0.0648 (287.5)	(+5.2'', +2.2'')	$\lesssim 15''$ (sm)	14P, ^{6m}
10173+0828	10 20 00.19	+08 13 34.5	0.0489 (214.4)	(0'', 0'')	$\lesssim 3''$ (co,cm)	23P, ^m ,13 ^m
10190+1322	10 21 42.60	+13 06 54.4	0.0765 (342.2)	(0'', 0'')	1.2'', 4''(co,dbl)	24P, ^m
10356+5345* (NGC 3310)	10 38 45.90	+53 30 11.7	0.0033 (14.0)	(0'', 0'')	50''(co,sm,x)	2P, ^m
10565+2448	10 59 18.15	+24 32 34.4	0.0428 (188.2)	(0'', 0'')	1.5''(co)	1P, ^m
11191+1200 (PG 1119+120)	11 21 47.12	+11 44 18.3	0.0500 (219.4)	(0'', 0'')	$\lesssim 5''$ (co)	25P, ^m
11231+1456* (IC 2810, UGC 6436)	11 25 45.00	+14 40 36.0	0.0341 (147.9)	(+1.2'', 0'')	6''(cm,sm)	21P,13 ^m ,26 ^m
11257+5850 (Arp 299)	11 28 32.45	+58 33 45.8	0.0103 (43.8)	(0'', 0'')	35''(co,sm,x)	27P, ^m ,6 ^m
12001+0215* (NGC 4045)	12 02 42.30	+01 58 38.0	0.0066 (28.4)	(-0.9'', -1.2'')	7''(cm)	21P,13 ^m
12112+0305	12 13 45.77	+02 48 39.3	0.0727 (324.4)	(+3.9'', +2.1'')	$\lesssim 2''$ (2.9''(co,dbl))	9P,18 ^m
12224-0624*	12 25 03.90	-06 40 53.0	0.0263 (113.4)	(0'', 0'')	$\lesssim 2''$ (cm)	21P,13 ^m
12243-0036* (NGC 4418)	12 26 54.70	-00 52 39.0	0.0073 (31.0)	(0'', 0'')	$\lesssim 3''$ (cm)	21P,13 ^m
12540+5708 (Mrk 231)	12 56 14.21	+56 52 25.1	0.0422 (184.1)	(0'', 0'')	0.85''(co)	1P, ^m
13001-2339*	13 02 52.10	-23 55 19.0	0.0215 (92.3)	(0'', 0'')	2''(ir)	5P,22 ^m
13102+1251* (NGC 5020)	13 12 39.90	+12 35 59.0	0.0112 (47.7)	(-1.0'', -0.9'')	12''(cm)	21P,13 ^m
Arp 238* (UGC 08335)	13 15 30.20	+62 07 45.0	0.0315 (136.3)	(0'', 0'')	5'' (35''(cm,dbl))	5P, 10 ^m
13183+3423 (Arp 193)	13 20 35.32	+34 08 22.2	0.0233 (100.2)	(0'', 0'')	1.5''(co)	1P, ^m
13188+0036* (NGC 5104)	13 21 23.10	+00 20 32.0	0.0186 (79.7)	(0'', 0'')	2.5''(cm)	21P,13 ^m
13229-2934 (NGC 5135)	13 25 43.97	-29 50 01.3	0.0136 (58.0)	(0'', 0'')	6''(cm)	10P, ^m
13362+4831 (NGC 5256)	13 38 17.90	+48 16 41.0	0.0278 (120.0)	(0'', 0'')	8''(cm, sm)	5P,13 ^m ,6 ^m
13428+5608 (Mrk 273)	13 44 42.12	+55 53 13.5	0.0378 (164.4)	(0'', 0'')	3''(co)	1P, ^m
13470+3530* (UGC 8739)	13 49 14.20	+35 15 23.0	0.0168 (71.9)	(-2.5'', +1.5'')	11''(cm,x)	21P,13 ^m
F13500+3141 (3C 293)	13 52 17.82	+31 26 46.4	0.0446 (194.9)	(0'', 0'')	7''(co)	28P, ^m
F13564+3741* (NGC 5394)	13 58 33.60	+37 27 13.0	0.0125 (53.3)	(0'', 0'')	5''(cm)	21P,13 ^m
14003+3245* (NGC 5433)	14 02 36.00	+32 30 38.0	0.0145 (61.9)	(0'', 0'')	8.5''(cm)	21P,13 ^m
14151+2705* (Mrk 673)	14 17 21.00	+26 51 28.0	0.0366 (159.0)	(0'', 0'')	$\lesssim 10''$ (opt)	5P, ^m
14178+4927* (Zw 247.020, Mrk 1490)	14 19 43.20	+49 14 12.0	0.0256 (110.3)	(0'', 0'')	2''(cm)	21P,13 ^m
14280+3126* (NGC 5653)	14 30 10.40	+31 12 54.0	0.0119 (50.7)	(-2.0'', +1.6'')	17''(cm)	21P, 13 ^m
14348-1447	14 37 38.32	-15 00 22.7	0.0825 (370.7)	(0'', 0'')	$\lesssim 2'', 3.5''$ (co,dbl)	29P, ^m ,13 ^m
15107+0724 (Zw 049.057)	15 13 13.07	+07 13 32.0	0.0129 (55.0)	(0'', 0'')	5''(co)	23P, ^m
15163+4255* (Mrk 848, Zw 107)	15 18 06.20	+42 44 42.0	0.0402 (175.1)	(0'', 0'')	7''(sm,cm)	5P, 6 ^m , 13 ^m
15243+4150* (NGC 5930, Arp 090)	15 26 07.90	+41 40 34.0	0.0089 (37.8)	(0'', 0'')	2.5''(cm)	21P,13 ^m
15322+1521* (NGC 5953p, Arp 091)	15 34 32.30	+15 11 38.0	0.0065 (27.6)	(0'', 0'')	10''(cm)	21P,13 ^m
15327+2340 (Arp 220)	15 34 57.24	+23 30 11.2	0.0182 (78.0)	(0'', 0'')	1.8''(co)	1P, ^m
15437+0234* (NGC 5990)	15 46 16.50	+02 24 56.0	0.0128 (54.6)	(-2.1'', -0.8'')	11''(cm)	21P,13 ^m
16104+5235* (NGC 6090, Mrk 496)	16 11 40.70	+52 27 25.0	0.0292 (126.1)	(0'', 0'')	6''(cm)	5P,13 ^m
16284+0411* (MCG +01-42-008)	16 30 56.50	+04 04 59.0	0.0245 (105.5)	(0'', 0'')	3.9''(cm)	21P,13 ^m
16504+0228 (NGC 6240)	16 52 59.05	+02 24 05.8	0.0243 (104.6)	(0'', 0'')	3''(co)	7P,30 ^m
17132+5313	17 14 20.48	+53 10 31.4	0.0507 (222.6)	(0'', +1.0'')	2.4''(cm)	31P,13 ^m
17208-0014	17 23 21.92	-00 17 00.7	0.0428 (186.8)	(0'', 0'')	1.7''(co)	1P, ^m

Table 3 – *continued* Observational parameters of the combined LIRG sample

Name ^a	RA (J2000) ^b	Dec (J2000) ^b	z (D _L) ^c	$(\Delta\theta_\alpha, \Delta\theta_\delta)^d$	$\langle\theta_s\rangle^e$	Refs ^f
18425+6036* (NGC 6701)	18 43 12.27	+60 39 10.5	0.0132 (56.3)	(+1.5'', +2.0'')	15''(cm)	9 ^p ,10 ^m
19458+0944	19 48 15.47	+09 52 01.3	0.1000 (454.8)	(0'', 0'')	$\lesssim 0.8''$ (ir)	14 ^p ,16 ^m
20550+1656* (II Zw 96)	20 57 23.70	+17 07 44.0	0.0363 (157.7)	(0'', 0'')	20''(sm,x)	5 ^p ,6 ^m
22491–1808	22 51 49.86	–17 52 24.4	0.0773 (346.0)	(–7.3'', 0'')	2.5''(ir,cm,x)	9 ^p ,15 ^m ,13 ^m
23007+0836 (NGC 7469)	23 03 15.60	+08 52 26.3	0.0163 (69.7)	(0'', 0'')	8''(co)	32 ^{p,m}
23365+3604	23 39 01.25	+36 21 08.4	0.0644 (285.6)	(0'', 0'')	0.95''(co)	1 ^{p,m}

^aIRAS name and the most common alternative(s), the asterisk marks sources for which CO line fluxes were obtained from an extensive literature search and line flux rectification process (see sections 2, 4.2).

^bSource coordinates (\mathbf{R}_{beam}) used for CO observations.

^cThe redshift used for receiver tuning (or the z_{CO} reported in the literature for LIRGs not in the original sample), and the corresponding luminosity distance in Mpc.

^dOffsets between expected CO source center \mathbf{R}_{cm} (assumed coincident with peak cm continuum) and observed position: $\Delta\mathbf{R}=\mathbf{R}_{\text{cm}}-\mathbf{R}_{\text{beam}}$ ($\Delta\mathbf{R}=\mathbf{0}$ when available CO or sub-mm images defined the CO source center, see 4.2). Thus \mathbf{R}_{cm} marks the true CO source center whenever $\Delta\mathbf{R}\neq\mathbf{0}$.

^eCO region angular size $\langle\theta_s\rangle=(\theta_{\text{min}}\theta_{\text{maj}})^{0.5}$, from interferometric maps. If these were not available then cm, near-IR, or sub-mm continuum images were used to set upper limits on $\langle\theta_s\rangle$. The qualifiers for the images used are: (co), (cm), (ir), (sm) for CO, cm, IR, and sub-mm images, (x)=complex source morphology ($\langle\theta_s\rangle$ then denotes the overall source size), (dbl)=double CO-bright nuclei. In the latter case $\langle\theta_s\rangle$ refers to the largest one, and the second number denotes their separation.

^fReferences used for source position (=p) and morphology/size (=m) information: 1=Downes & Solomon 1998; 2=Zhu et al. 2009; 3=Schinnerer et al. 1998; 4=Eckart et al. 1994; 5=Leech et al. 2010; 6=Mortier et al. 2009; 7=Wang et al. 1991; 8=Casoli et al. 1992; 9=Sanders et al. 1991; 10=Condon et al. 1996; 11=Appleton et al. 2002; 12=Papadopoulos & Seaquist 1998a; 13=Condon et al. 1990; 14=Solomon et al. 1997; 15=Scoville et al. 2000; 16=Murphy et al. 1996; 17=Bryant & Scoville 1999; 18=Evans et al. 2002; 19=Sanders et al. 1988; 20=Wilson et al. 2008; 21=Yao et al. 2003; 22=Zenner & Lenzen 1993; 23=Planesas et al. 1991; 24=Gracia-Carpio et al. 2007; 25=Evans et al. 2001; 26=Lisenfeld et al. 2000; 27=Aalto et al. 1997; 28=Evans et al. 1999; 29=Evans et al. 2000; 30=Tacconi et al. 1999; 31=Young et al. 1995; 32=Davies et al. 2004; 33=Crawford et al. 1996

^gDouble nuclei in near-IR (Scoville et al. 2000), but only one is CO-bright (Evans et al. 2002).

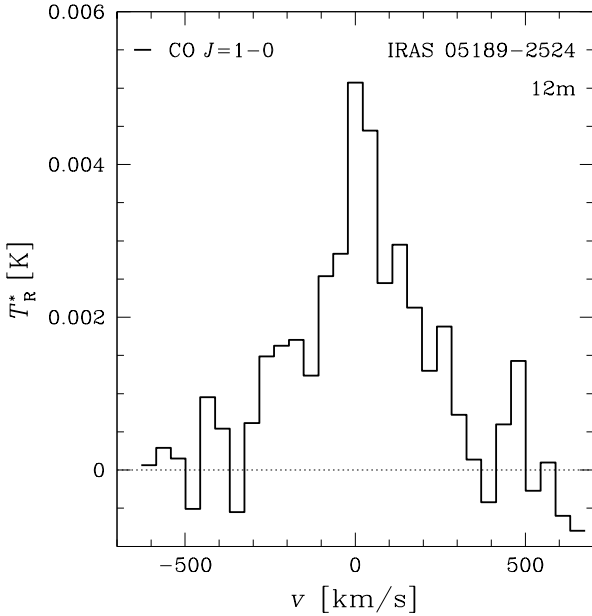


Figure 4. The CO J=1–0 spectrum of IRAS 05189–2524, centered at $v=12800$ km s^{–1}, obtained with the 12 m telescope (see section 4.2.1).

Indicatively, even for the ULIRG/QSO Mrk 231 where ground and Herschel/FTS observations completed its CO SLED from J=1–0 up to J=13–12 (van der Werf et al. 2010) it is always $r_{J+1,J} < r_{J,J-1}$.

5.1 Very high excitation gas: “out-exciting” Orion A and B

The qualitatively different state of the molecular gas in (U)LIRGs than in spiral disks, has been noted in the past by several groups (e.g. Aalto et al. 1995; Solomon et al. 1997; Downes & Solomon 1998; Papadopoulos & Seaquist 1998; Yao et al. 2003). Moreover ISM conditions similar to those in ULIRGs have been revealed in the nuclei of nearby spirals but involving only small fractions of their total molecular gas (e.g. Bradford et al. 2003). Nevertheless most such studies lacked J=3–2 and higher-J CO lines, and did not benchmark their very limited CO SLEDs to any regions where excitation mechanisms are well-determined (e.g. SF hot-spots in Galactic GMCs).

For the highly excited CO SLEDs of some ULIRGs a superposition of two optically thick CO SLEDs, a high-excitation and a low-excitation one, can at most yield a “flattening” or a slower decline of high-J CO line ratios with respect to those expected from a low-excitation phase. Only dense and warm gas with at least partially optically thin CO lines can produce $r_{43} > r_{32}$ and/or $r_{32} > r_{21}$ and the high excitation tails seen in Figure 5 ($r_{21,32} > 1$). Such CO line ratios are rare, and reported in the past only for the starburst nuclei of M 82 and NGC 3310 (Knapp et al. 1980; Olofsson & Rydbeck 1984; Braine et al. 1993), and although confirmed at lower values, they are still > 1 (Weiss et al. 2001; Zhu et al. 2009), implying extraordinary ISM conditions. Our study recovers this as a statistically robust result for our sample. Indeed, while measurement errors still allow $r_{J+1,J} \lesssim 1$ for individual objects with measured $r_{J+1,J} > 1$ (J=1,2), this cannot be so for all the LIRGs in the high excitation tails in Figure 5 as the probability for this is: $P_{21} \sim 5 \times 10^{-7}$ and $P_{32} \sim 4.4 \times 10^{-7}$ for the (2–1)/(1–0) and (3–2)/(1–0) line ratios (assuming independent gaussian probability distributions for each measurement). Thus some extraordinary physical conditions are possible for the *bulk* of the molecular gas of some (U)LIRGs.

Table 4. ^{12}CO J=1-0, 2-1, 3-2 data for the combined LIRG sample

Name	CO J=1-0 ^a	CO J=2-1 ^a	CO J=3-2 ^a	Refs. ^b
00057+4021	46 ± 7	178 ± 30	267 ± 45(1.087, G)	x,1
00322-0840*	500 ± 125 ^c	2000 ± 500 ^c	2610 ± 650 ^c	2
00509+1225	34 ± 7(1.11, K _c)	114 ± 23(1.11, K _c)	356 ± 103(1.27, K _c)	x,3
01053-1746*	691 ± 138		3324 ± 660	4,5
01077-1707*	178 ± 36		507 ± 100	4,5
01418+1651*	75 ± 15		417 ± 83	4,5
02071+3857	408 ± 33	1238 ± 248 ^d	2560 ± 515	x,6
02080+3725*	147 ± 29		586 ± 115(1.052, K _{sh})	6,7
02114+0456*	159 ± 32		1196 ± 240	4,5
02321-0900	49 ± 6	215 ± 35(1.387, K _c)	245 ± 55(2.087, K _c) ^e	x,8,9
02401-0013*	2830 ± 424	(1.13 ± 0.22) × 10 ⁴	(1.71 ± 0.34) × 10 ⁴	10 ^f
02483+4302	30 ± 4	116 ± 21	119 ± 17(1.087, G)	x,1,4,11
02512+1446*	194 ± 39		387 ± 77	4,5
03359+1523	155 ± 23 ^g		256 ± 51	4,7
04232+1436	34 ± 7		335 ± 76	x,11
05083+7936	87 ± 9	252 ± 33	340 ± 145(1.087, G)	x,1,11,12
05189-2524	48 ± 7	130 ± 22(1.10, K _{sh})	256 ± 36(1.27, K _{sh})	x
08030+5243	30 ± 6	77 ± 12	98 ± 17(1.087, G)	x,11
08354+2555*	162 ± 20	267 ± 40 ⁱ	614 ± 92	7,13,14,15
08572+3915	10.5 ± 1.5	41 ± 12	≤ 240 ^h	x,11,16
09126+4432	162 ± 23	779 ± 126(3.08, K _c) ^j	775 ± 130	x,4,7,14,17
“ “ (SW nucleus)			540 ± 61	x,4
“ “ (NE nucleus)			235 ± 40	x,4
09320+6134	70 ± 14	345 ± 62	589 ± 95(1.087, G)	x,11
09586+1600*	126 ± 26(1.086, K _{sh})		837 ± 126(1.086, K _{sh})	x,6,18
10039-3338*	65 ± 14		316 ± 65	4,5
10035+4852	48 ± 10(1.20, K _{sh})	168 ± 29(1.20, K _{sh})		x,11
10173+0828	56 ± 10		127 ± 24 (1.087, G)	x,7,18
10190+1322	37 ± 7	100 ± 20(1.06, K _c)	225 ± 37	x,4,19
10356+5345*	140 ± 28 ^c	822 ± 166	1525 ± 300 ^c	2
10565+2448	77 ± 8	327 ± 35	560 ± 56	x,1,4,7,11,18,20
11191+1200	4.5 ± 0.8		22 ± 5(1.045, K _c)	x,21
11231+1456*	145 ± 20		413 ± 87(1.07, K _c)	7,18
11257+5850	586 ± 115		4360 ± 655	x,4,5,15,22
12001+0215*	138 ± 28		311 ± 65	18
12112+0305	42 ± 5	152 ± 30(1.45, K _{sh})	598 ± 113(1.26, K _{sh})	x,7,16
12224-0624*	22 ± 9		235 ± 52	18
12243-0036*	132 ± 28		995 ± 204	18
12540+5708	88 ± 9	315 ± 30	568 ± 80	23
13001-2339*	152 ± 30		864 ± 173	4,5
13102+1251*	94 ± 19		424 ± 90	18
Arp 238*	110 ± 22		300 ± 60	4,5
13183+3423	194 ± 16	850 ± 130	1294 ± 171(1.087, G)	x,1,7,11,13,18,24,25
13188+0036*	150 ± 30		706 ± 143	18
13229-2934	382 ± 48	1236 ± 120	1960 ± 295 ^k	x,26
13362+4831	175 ± 20		912 ± 90 ^k	x,4,5,14,17
13428+5608	82 ± 9	270 ± 35	482 ± 82(1.087, G)	x,1,7,11
13470+3530*	118 ± 24(1.11, K _{sh})		1126 ± 231(1.11, K _{sh})	18
F13500+3141	52 ± 8	155 ± 28(1.035, K _c)	208 ± 55(1.09, K _c)	x,27
F13564+3741*	244 ± 51		756 ± 150	18
14003+3245*	58 ± 17		853 ± 181	18
14151+2705*	78 ± 16		340 ± 70	4
14178+4927*	68 ± 15		544 ± 115	18
14280+3126*	187 ± 27		806 ± 162	7,18
14348-1447	56 ± 8	212 ± 35	360 ± 67	x,7,28,29
15107+0724	120 ± 11	605 ± 92	710 ± 100(1.045, K _c)	x,7,14,18,30
15163+4255*	114 ± 23		364 ± 73	4,5
15243+4150*	52 ± 14		246 ± 55	18
NGC 5953p*	110 ± 24		813 ± 166	18
15327+2340	419 ± 36	1127 ± 69	3674 ± 405	31
15437+0234*	224 ± 52(1.077, K _{sh})		636 ± 133(1.077, K _{sh})	18
16104+5235*	155 ± 31		1062 ± 212	4,5
16284+0411*	63 ± 15		580 ± 120	18

Table 4 – *continued* ^{12}CO J=1–0, 2–1, 3–2 data for the combined LIRG sample

Name	CO J=1–0 ^a	CO J=2–1 ^a	CO J=3–2 ^a	Refs. ^b
16504+0228	322 ± 29	1492 ± 253	3205 ± 642	31
17132+5313	127 ± 18	168 ± 29	264 ± 48	x,14,17
17208–0014	160 ± 16	688 ± 109	1198 ± 190(1.087, G)	x,1,11,29,30
18425+6036*	234 ± 47		1440 ± 288	6,7
19458+0944	29 ± 6		261 ± 65(1.087, G)	x,11
20550+1656*	121 ± 24		527 ± 105	4,5
22491–1808	33 ± 6	145 ± 34(1.36, K _{sh})	558 ± 190(2.1, K _{sh}) ^l	x,7
23007+0836	298 ± 27	890 ± 103	1600 ± 240(1.12, K _c)	x,7,13,14,26,32,33,34
23365+3604	39 ± 6	117 ± 20	288 ± 71(1.087, G)	x,1,11

^aVelocity-integrated line flux densities in Jy km s^{-1} , with the value and type of any applied corrections reported in the parentheses (see 4.1), G: the pointing error bias, $K_{\text{sh}}=K_{\text{sh}}(\Delta\theta)$ (with $\Delta\theta=[(\Delta\theta_{\alpha})^2+(\Delta\theta_{\delta})^2]^{1/2}$): position offset correction, K_c : beam-source geometric coupling correction for sources with *known* CO or sub-mm dust emission source size θ_s .

^bx=this work, 1=Downes & Solomon 1998; 2=Zhu et al. 2009; 3=Barvainis et al. 1989; 4=Leech et al. 2010; 5=Gao et al. 1999; 6=Narayanan et al. 2005; 7=Sanders et al. 1991; 8=Alloin et al. 1992; 9=Appleton et al. 2002; 10=Papadopoulos & Seaquist 1998a; 11=Solomon et al. 1997; 12=Scoville et al. 1989; 13=Bryant & Scoville 1999; 14=Young et al. 1995; 15=Wilson et al. 2008; 16=Evans et al. 2002; 17=Sanders et al. 1986; 18=Yao et al. 2003; 19=Gracia-Carpio et al. 2007; 20=Bayet et al. 2006; 21=Evans et al. 2001; 22=Casoli et al. 1992; 23=Papadopoulos et al. 2007; 24=Evans et al. 2005; 25=Mazzarella et al. 1993; 26=Papadopoulos & Seaquist 1998b; 27=Evans et al. 1999; 28=Evans et al. 2000; 29=Mirabel et al. 1990; 30=Planesas et al. 1991; 31=Greve et al. 2009; 32=Davies et al. 2004; 33=Meixner et al. 1990; 34=Papadopoulos & Allen 2002

^cJ=1–0, 3–2 for the central 40'', J=2–1 for the inner 20'' (from Zhu et al. 2009).

^dFrom CO J=1–0 and the $\langle(2-1)/(1-0)\rangle$ ratio over the inner 22'' (Casoli et al. 1992).

^eProbably an underestimate (source significantly larger than the JCMT beam).

^fFluxes for the inner 20'' of the galaxy.

^gShift factor $K_{\text{sh}}=1.25$ applied for the Sanders et al. 1991 value.

^h 3σ upper limit.

ⁱFlux from an SMA image most likely collecting all of it given its single dish CO 3–2 flux is also recovered by the interferometer.

^jUncertain value, large correction of a single CO 2-1 observation of a widely separated pair, pointing $\sim 6''$ away from SW nucleus.

^kA 3×3 grid map at 7'' grid size was made to obtain total line flux.

^lA large correction factor makes this value uncertain.

In the Galaxy such high CO line ratios are found *only* in isolated “hot” spots in GMCs as results of strong and very localized excitation mechanisms. These are intense far-UV radiation from O,B stars inducing Photon-dominated Regions (PDRs) containing warm gas near HII regions (Sakamoto et al. 1994), or supernovae remnant (SNR)-induced shocks (e.g. Seta et al. 1998; Arikawa et al. 1999; Bolatto et al. 2003) which yield warm and strongly kinematically stirred gas ($K_{\text{vir}} \gg 1$). In the Orion A, B molecular clouds, the site of active formation of O, B stars in the Galaxy, the cloud-average $\langle r_{21} \rangle_{A,B} \sim 0.62-0.75$, with $r_{21} \sim 0.90-1.3$ found only in few isolated PDRs near HII regions and O, B star associations (Sakamoto et al. 1994). Thus $r_{21} \gtrsim 0.8$, observed in several LIRGs, already places their entire molecular gas reservoirs higher than the Orion A, and B clouds in terms of average excitation, while $r_{21} > 1$ puts them on par with their “hottest” SF spots and the excitation state of molecular gas in SNR-GMC interfaces! This is indeed extraordinary given that the extreme conditions needed to produce optically thin CO lines in LIRGs must then be maintained over large molecular gas reservoirs ($\sim 10^9-10^{10} M_{\odot}$). The CO/ ^{13}CO J=1–0, 2–1 line ratios (Figure 7), with $\langle R_{10} \rangle \sim \langle R_{21} \rangle = 18$, are significantly larger than typical GMCs in the Galactic disk ($R_{10} \sim 4-6$, e.g. Solomon et al. 1979; Polk et al. 1988), and independently indicate low optical depths. Using again the Orion A and B clouds to indicate how extraordinary such large $R_{10,21}$ ratios are for galaxy-sized molecular gas reservoirs we note that $R_{21}=10$ is observed only in

“hot” isolated interfaces of molecular gas to O,B stellar associations while for the bulk of the gas in Orion $R_{21} \sim 4-6$ (Sakamoto et al. 1994). Even in the highly turbulent and warm molecular clouds in the Galactic Center the CO line emission remains mostly optically thick with $R_{10} \sim 5$ and $\tau_{10} \sim 5$ (Oka et al. 1998). In other galactic nuclei such a dense and warm gas phase amounts to only $\sim (1-2)\%$ of the total molecular gas mass of a typical spiral disk.

The extreme thermal and/or kinematic conditions needed to achieve even partially optically thin CO SLEDs can be simply demonstrated using the CO J=1–0 optical depth:

$$\tau_{10} = \frac{c^3 g_1 A_{10}}{8\pi\nu_{10}^3} \left(\frac{1 - e^{-E_{10}/k_B T_k}}{Z_{\text{LTE}}} \right) \left[\frac{\text{CO}}{\text{H}_2} \right] \frac{n(\text{H}_2)}{(\text{dV}/\text{dr})}, \quad (8)$$

(assuming LTE), where Z_{LTE} is the partition function. After substituting the various physical constants this becomes

$$\tau_{10} = 1.29 \times 10^4 \left(\frac{1 - e^{-5.5/T_k}}{T_k} \right) \left[\frac{\text{CO}}{\text{H}_2} \right] \frac{n(\text{H}_2)}{(\text{dV}/\text{dr})}, \quad (9)$$

where dV/dr is in units of $\text{km s}^{-1} \text{pc}^{-1}$. For $[\text{CO}/\text{H}_2] \sim 10^{-4}$ (for Solar metallicities), and setting the average velocity gradient of the gas phase as $(\text{dV}/\text{dr}) = K_{\text{vir}} \times (\text{dV}/\text{dr})_{\text{vir}}$ where

$$\left(\frac{\text{dV}}{\text{dr}} \right)_{\text{vir}} \approx 0.65 \sqrt{\alpha} \left(\frac{n(\text{H}_2)}{10^3 \text{cm}^{-3}} \right)^{1/2} \text{ km s}^{-1} \text{ pc}^{-1}, \quad (10)$$

is the average velocity gradient expected for a virialized gas phase

Table 5. The CO J=4–3, 6–5 data

Name	CO J=4–3 ^a	CO J=6–5 ^a
00057+4021	1049 ± 370 (1.15, G)	≲ 380 ^b (1.29, G)
00509+1225		430 ± 155 (1.97, G) ^c
02483+4302		401 ± 131 (1.27, G)
04232+1436		≲ 345 ^b (1.21, G)
05083+7936	2033 ± 593 (1.15, G)	688 ± 207 (1.22, G)
05189–2524	≲ 689 ^b (1.47, K _{sh})	638 ± 220 (1.21, G)
08572+3915 (NW nucleus)		405 ± 158 (1.21, G)
09126+4432 (NE nucleus)		705 ± 230 (1.90, K _{sh}) ^d
09320+6134		≲ 422 ^b (1.35, G)
10173+0828		≲ 156 ^b (1.27, G)
10565+2448		506 ± 148 (1.35, G)
11257+5850	6340 ± 1585 ^e	
11191+1200		261 ± 82 (1.14, K _c)
12112+0305 (NE nucleus)		327 ± 143 ^f (1.22, G)
12112+0305 (SW nucleus)		≲ 123 ^b (1.21, G)
12540+5708	1127 ± 265 (1.15, G)	1320 ± 400 (1.29, G)
13183+3423		≲ 630 ^b (1.28, G)
13428+5608		488 ± 156 (1.45, G)
F13500+3141	842 ± 245 (1.15, K _c)	1086 ± 347 (1.29, K _c)
15107+0724	1122 ± 262 (1.073, K _c)	904 ± 241 (1.14, K _c)
15237+2340		3130 ± 810 (1.21, G)
16504+0228		3321 ± 860 (1.21, G)
17208–0014	2312 ± 654 (1.15, G)	340 ± 140 ^g (1.17, G)
23007+0836	3970 ± 820 (1.19, K _c)	2355 ± 590
23365+3604	≲ 489 ^b (1.15, G)	295 ± 110 (1.37, G) ^g

^aVelocity-integrated line flux densities in Jy km s^{−1}, with the value and type of any corrections applied (section 4.1) reported in the parentheses. A few CO J=6–5 fluxes differ slightly from those in P10b, a result of additional data.

^b3σ upper limit.

^cThe high velocity part of a double horn line tentatively detected, large correction applied because of extended source, uncertain total line flux.

^dPossible detection, highly uncertain because a pointing offset of ∼3.85'' results to a beam-shift correction K_{sh}=1.90.

^eFrom a partially completed CO J=4–3 map, and thus a likely underestimate.

^fTentative detection of the NE nucleus of a double source.

^gVery uncertain value.

(with $\alpha \sim 0.5$ –2.5 depending on the assumed cloud density profile, Greve et al. 2009; Bryant & Scoville 1996), we obtain

$$\tau_{10} = 63\alpha^{-1/2} \left(\frac{1 - e^{-5.5/T_k}}{T_k} \right) \frac{\sqrt{n(\text{H}_2)}}{K_{\text{vir}}}. \quad (11)$$

For most gas in typical GMCs: $T_{\text{kin}} \sim (15\text{--}30)$ K, $n(\text{H}_2) \sim (500\text{--}10^3)$ cm^{−3}, and $K_{\text{vir}} \sim 1$ (virial gas motions), yielding $\tau_{10} \sim 6.5\text{--}33$ (for $\alpha=1.5$). Only high temperatures ($T_{\text{kin}} \gtrsim 100$ K) and/or highly non-virial gas motions ($K_{\text{vir}} \gtrsim 10$) can produce $\tau_{10} \lesssim 1$. Moreover the conditions necessary for $r_{J+1,J} > 1$ become even more extreme for higher-J lines since, along with the high temperatures needed (so that $E_{J+1,J}/(k_B T_k) \ll 1$), such ratios need densities high enough to thermalize the J+1→J line while retaining moderate/low optical depths. The latter becomes progressively more difficult for higher-J lines since $\tau_{J+1,J} \sim (J+1)^2 \tau_{10}$ (for LTE and $E_{J+1,J}/(k_B T_k) \ll 1$). Thus to keep $\tau_{10} \ll 1$ (so that e.g. $\tau_{43} \sim 16\tau_{10}$ will remain $\lesssim 1$ yielding an optically thin J=4–3 line) both high T_{kin} and highly non-virial gas motions are necessary. Indeed for $T_k=100$ K, Equation 11 yields $\tau_{10} \sim 2.8 \times 10^{-2} K_{\text{vir}}^{-1} \sqrt{n(\text{H}_2)}$, which for $n(\text{H}_2) > (1\text{--}2) \times 10^4$ cm^{−3} (the critical densities of the J=3–2, 4–3 lines) gives $\tau_{10} \gtrsim (3\text{--}4) K_{\text{vir}}^{-1}$, which can be brought into

the optically thin regime provided that $K_{\text{vir}} \gtrsim 10$, which corresponds to highly unbound dynamical states for the gas.

As the star-forming Orion A and B molecular clouds demonstrate, with low CO line excitation and large optical depths prevailing when averaged over their entire volume, such extreme conditions cannot easily dominate the CO SLEDs of individual SF clouds let alone the global CO SLEDs of entire galaxies. Thus $r_{J+1,J} \gtrsim 1$ (J=1,2,3) ratios are not expected, even in vigorously star-forming LIRGs, and are indicative of strong *galaxy-wide* effects maintaining high gas temperatures as well as highly non-virial velocity fields up to densities $n > 10^4$ cm^{−3} throughout their large molecular gas reservoirs. As we will argue in more detail later such a high-excitation gas phase is irreducible to an ensemble-average of individual SF molecular clouds. For the rest of LIRGs more ordinary excitation states of SF ($r_{21,32} \lesssim 0.9$) and non-SF ($r_{21} \sim 0.5\text{--}0.7$, $r_{32} \sim 0.3$) gas adequately account for their observed CO SLEDs.

High resolution submm imaging with ALMA will reveal extreme CO line excitation and thus extraordinary ISM conditions much more frequently as the high CO ratios of SF-powered regions or AGN-excited gas will no longer be “watered-down” by lower-excitation cloud ensembles. Line ratio imaging can then reveal deeply dust-enshrouded AGN in galactic centers where nei-

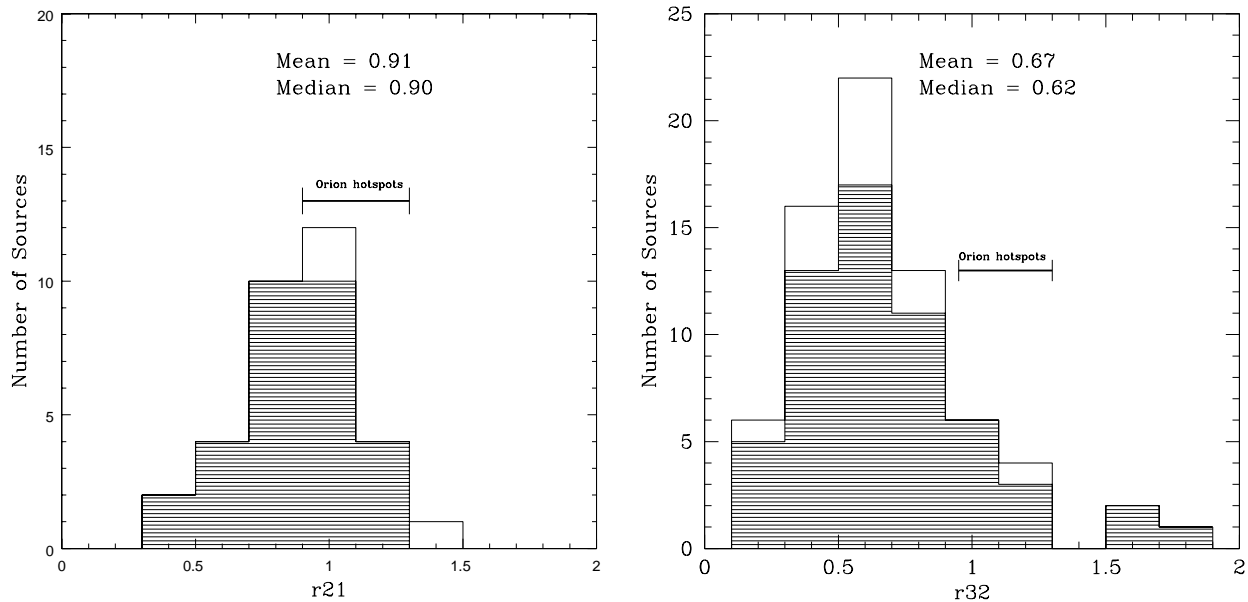


Figure 5. The distributions of the CO (2–1)/(1–0) (left) and (3–2)/(1–0) (right) global brightness temperature ratios for the LIRGs in our sample. The shaded area marks the line ratio distributions for sources with CO emission region angular sizes of $\leq 15''$ (the HPBW of the JCMT at 345 GHz). The measured range of the (2–1)/(1–0) line ratio in the hot spots near H II regions or PDRs around O, B stars in the Orion A, and B molecular clouds (Sakamoto et al. 1994), and the expected range of the CO (3–2)/(1–0) ratio in these high-excitation regions are indicated by the horizontal bar.

ther optical nor even IR lines are capable of doing so. An early such demonstration is the imaging of the central ~ 100 pc of grand design spiral galaxy M51 which finds high CO line excitation with $r_{32} \sim 1.9$, and possibly caused by an AGN-powered jet (Matsushita et al. 2004).

5.2 High-excitation gas in LIRGs: “bottom”-stirred by SF feedback?

A warm ($T_{\text{kin}} \gtrsim 100$ K) unbound ($K_{\text{vir}} \gg 1$) phase concomitant with a less excited cooler and denser one is a feature of standard two-phase models in (U)LIRGs (e.g. Aalto et al. 1995; Papadopoulos & Seaquist 1999), and could in principle explain the very high-excitation CO SLEDs in our sample. In these systems a frequent non-convergence of global CO line ratios (mostly CO, ^{13}CO 1–0, 2–1) to an average ISM state is attributed to an envelope-like diffuse ($n \sim (10^2\text{--}10^3) \text{ cm}^{-3}$) non self-gravitating warm gas with high turbulent linewidths (and thus small/moderate τ_{10}), surrounding much denser self-gravitating gas where CO and even ^{13}CO lines have large optical depths (Aalto et al. 1995). However, the difficulty of maintaining low optical depths *and* well-excited CO J=3–2, 4–3 lines (so that $r_{43,32} \gtrsim 1$) makes this two-phase ISM model problematic as the “envelope” phase should then have $n(\text{H}_2) > 10^4 \text{ cm}^{-3}$ ($n_{\text{crit}}(3\text{--}2, 4\text{--}3) \sim (1\text{--}2) \times 10^4 \text{ cm}^{-3}$) rather than $n \lesssim 10^3 \text{ cm}^{-3}$.

SF-feedback effects capable of producing highly-excited CO SLEDs with moderate/low optical depths up to J=3–2, 4–3 do occur in dense gas regions deep inside molecular clouds, and are driven by the massive stars. The warm PDRs and SNR-shocked gas regions, along with strong radiation pressure onto the dust grains mixed with the molecular gas can produce a warm *and* non self-gravitating ($K_{\text{vir}} > 1$) dense phase near SF sites. It is worth noting that radiation pressure from massive stars is powerful enough to even be the main SF-regulator in the starbursts found in ULIRGs (Andrews & Thompson 2011). Such a “bottom”-stirred ISM would

yield a very different two-phase differentiation, with a warm, dense, and non-virial phase lying deeply embedded in molecular clouds, surrounded by a less dense cooler one extending further from the vicinity of SF sites. A warm, dense, and non-virial phase is indeed compatible with the CO line ratios of the SF “hot-spots” of Orion A,B molecular clouds (see 7.2.1), with CO SLEDs expected to be highly excited and partially optically thin up to high-J lines, a result of the high temperatures and K_{vir} values.

5.2.1 A “bottom”-stirred ISM, some predictions

In the context of the old 2-phase model, the high CO/ ^{13}CO J=1–0 ratios in ULIRGs ($R_{10} \gtrsim 20$) are attributed to the much more turbulent ($K_{\text{vir}} \gg 1$) diffuse/warm “envelopes” than those of molecular clouds in less extreme star-forming systems ($R_{10} \sim 10\text{--}15$) or SF-quiet ones like the Milky Way ($R_{10} \sim 4\text{--}6$) (Aalto et al. 1995). A much larger amount of turbulent energy per gas mass is available in ULIRGs, a result of strong mergers, and its dissipation can readily warm molecular gas (Pan & Padoan 2009) and increase R_{10} . In a “bottom”-stirred ISM however, the dense phase is the one most affected by the SF feedback and thus *high* ($\gtrsim 15$) $^{12}\text{CO}/^{13}\text{CO}$ $R_{J+1,J}$ $J+1=3, 4, 5, 6$ and $\text{HCN}/\text{H}^{13}\text{CN}$ $J=1\text{--}0$ ratios are expected, as dense gas can now attain low/moderate molecular line optical depths. These transitions (which would be very optically thick for dense gas that has $K_{\text{vir}} \sim 1$), with $n_{\text{crit}} \sim (10^4\text{--}10^5) \text{ cm}^{-3}$, probe the dense gas with negligible contributions from diffuse cloud envelopes. High C^{13}C -based isotopologue line ratios at ever increasing critical densities (e.g. $\text{HCN}/\text{H}^{13}\text{CN}$ J=3–2, $n_{\text{crit}} \sim 4 \times 10^6 \text{ cm}^{-3}$) would then provide an ever sharpening distinction between a “bottom”-stirred and a standard two-phase ISM model in (U)LIRGs.

Table 6. The ^{13}CO line data

Name	$^{13}\text{CO J=1-0}^a$	$^{13}\text{CO J=2-1}^a$	References ^b
00057+4021		$\lesssim 24^c$	this work
00509+1225	4.0 ± 0.8	$(R=6 \pm 2)^d$	1, this work
01053-1746*	$(R \gtrsim 17)^{c,d}$		2
02071+3857	37 ± 6	$(R=12 \pm 3)^d$	this work
02401-0013*	185 ± 28	1034 ± 200	5
02483+4302	$\lesssim 2.1^c$	$\lesssim 21^c$	this work
03359+1523		$(R=12 \pm 3)^e$	this work
05083+7936	7.9 ± 2.3	23.0 ± 4.5	this work
05189-2524		21 ± 7	this work
08354+2555		$(R \gtrsim 18)^{c,d}$	6
09126+4432		$\lesssim 55^c$	this work
09320+6134		18 ± 3	this work
10035+4852		9.9 ± 2.5^f	this work
10173+0828		5.2 ± 1.0	this work
10565+2448	4.7 ± 1.3	$(R \gtrsim 18)^c$	this work, 6
11257+5850	$(R=27 \pm 5)^d$		7
12540+5708		6.1 ± 2.1	this work
13183+3423		26 ± 4	this work
13229-2934	13.5 ± 2.0	87 ± 13	this work, 8
13428+5608		36 ± 9	this work
F13500+3141	$\lesssim 11.8^c$		this work
14348-1447		16.7 ± 5.6	this work
15107+0724	6.8 ± 1.8	23 ± 7	this work
15327+2340	9 ± 2	59 ± 7	this work, 9
16504+0228	6.5 ± 1.9	26 ± 4	this work, 9
17208-0014		$\lesssim 18^c$	this work
23007+0836		54 ± 13	8
23365+3604		6.2 ± 1.4	this work

^aThe velocity-integrated line flux densities in Jy km s^{-1} .

^b1=Eckart et al. 1994; 2=Aalto et al. 1995; 3=Aalto et al. 1991; 4=Casoli et al. 1992; 5=Papadopoulos & Seaquist 1998a; 6=Wilson et al. 2008; 7=Aalto et al. 1997; 8=Papadopoulos & Seaquist 1998b; 9=Greve et al. 2009.

^c 3σ upper limit.

^dOnly $R=^{12}\text{CO}/^{13}\text{CO}$ is available (reported in parenthesis) for areas smaller than the total CO-emitting region (see 4.2).

^eLarge pointing offset for both CO and ^{13}CO line measurements makes absolute fluxes uncertain but leaves line ratio invariant.

^fUncertain value, large K_{sh} correction applied ($K_{\text{sh}}=2$).

5.3 The quest for a new ISM excitation mechanism in ULIRGs

The small amount of gas mass typically found in the SF “hot-spots” of ordinary star-forming GMCs renders even a “bottom”-stirred ISM model problematic in producing the highest excitation CO SLEDs found in our sample. Indeed, even if all the dense gas ($>10^4 \text{ cm}^{-3}$) in GMCs was feedback-affected it would still amount only to \sim few% of their total mass. This cannot “skew” their CO SLED anywhere close to the high excitation levels observed for some ULIRGs (e.g. IRAS 12112+0305, IRAS 17208-0014). *Much larger mass fractions of GMCs must be dense and SF-active for such SLEDs to emerge.* High cloud boundary pressures and tidal stripping of outer GMC envelopes in a merger environment can produce much denser clouds, a situation exemplified by the Galactic Center (Güsten & Phillip 1994). Large amounts of molecular gas ($\sim 10^{10} M_{\odot}$) at densities $\sim (10^5\text{-}10^6) \text{ cm}^{-3}$, and a possible steepening of the (average density)-size power law $\langle n \rangle \propto L^{-k}$ to $k > 1$ ($k=1$ for Galactic GMCs, Larson 1981) certainly argue for a much denser molecular ISM in ULIRGs (Greve et al. 2009). At the same

time this hinders far-UV photon propagation even more (i.e. the PDRs will be smaller) while SNR-induced shocks in such dense ISM will dissipate fast and produce shock-excited molecular gas regions that are even more confined around the SNR sites. Thus *a quest for mechanisms that can globally heat the large amounts of dense gas found in ULIRGs to high temperatures opens up.*

5.4 Strong AGN feedback: a new global driver of ISM excitation

Two intriguing objects, the optically/IR-luminous QSO PG 1119+120, and the powerful FR II radio galaxy 3C 293, widen the range of possibilities regarding globally operating molecular gas excitation mechanisms in galaxies. This is particularly clear in 3C 293 where a strong jet-ISM interaction injects large amounts of mechanical energy into its highly turbulent ISM and powers luminous CO J=4-3, 6-5 lines in an otherwise SF-quiet ISM with subthermal low-J CO line ratios and cold dust emission (Papadopoulos et al. 2008, 2010b). Strong, penetrating irradiation by an X-ray luminous AGN can volumetrically heat molecular gas by creating giant X-ray Disassociation Regions (XDRs), and is another powerful and possibly global ISM excitation mechanism in AGN-hosting LIRGs (Meijerink et al. 2007; Schleicher et al. 2010). Unfortunately there are no X-ray observations of PG 1119+120 to assess the X-ray luminosity of its AGN, while we find no particular predominance of AGN amongst the LIRGs populating the high-excitation tails in Figure 5. Very high-J CO SLEDs ($J \geq 8-10$) will provide the tools for distinguishing between AGN-induced XDRs, SF-induced PDRs as the cause of high ISM excitation (Meijerink et al. 2006; van der Werf et al. 2010). Finally the recent discovery of a massive molecular gas outflow, likely driven by the AGN in Mrk 231, by Aalto et al. (2012) inserts an exciting new element in this debate by demonstrating that much higher density gas ($>10^4 \text{ cm}^{-3}$) can also be affected by AGN feedback.

6 CO LINE RADIATIVE TRANSFER MODELS

Interpreting global CO line ratios in terms of underlying *average* gas physical conditions is the task of molecular line radiative transfer models. In the present analysis of the CO, ^{13}CO lines we will use a Large Velocity Gradient code (see Papadopoulos & Seaquist 1998 and references therein) that has been shown adept at discerning the average thermal and kinematic states of the molecular gas when constrained by CO, ^{13}CO line ratios (e.g. Mao et al. 2000; Weiss et al. 2001; Yao et al. 2003). Our LVG code uses the observed CO ratios $R_k^{(\text{obs})}$ to find the regions in the $[n(\text{H}_2), T_k, \Lambda_{\text{CO}}]$ parameter space where $\chi^2 = \sum_k (1/\sigma_k)^2 [R_k^{(\text{obs})} - R_k]^2$ (where R_k is a model line ratio and σ_k the measurement error) is minimum. $\Lambda_{\text{CO}} = [\text{CO}/\text{H}_2]/(dV/dR)$ (in $(\text{km s}^{-1} \text{ pc}^{-1})^{-1}$), where $[\text{CO}/\text{H}_2]$ is the CO abundance and dV/dR is the average local velocity gradient of the turbulent CO line emitting gas. The temperature range we considered is: $15 \text{ K} \leq T_{\text{kin}} \leq 150 \text{ K}$, with the minimum value typical of cold SF-quiet gas and the maximum of the Cold Neutral Medium HI. Moreover only LVG solutions with $K_{\text{vir}} \gtrsim 1$ where

$$K_{\text{vir}} = \frac{(dV/dR)}{(dV/dR)_{\text{virial}}} \sim 1.54 \frac{[\text{CO}/\text{H}_2]}{\sqrt{\Lambda_{\text{CO}}}} \left(\frac{n(\text{H}_2)}{10^3 \text{ cm}^{-3}} \right)^{-1/2} \quad (12)$$

(using equation 10) are accepted. The latter determines the average dynamic state of the molecular gas, with $K_{\text{vir}} \sim 1-3$ for the

Table 7. ^{12}CO line ratios and SF-powered IR luminosities

Name	r_{21}^a	r_{32}^a	r_{43}^a	r_{65}^a	$L'_{\text{CO}(1-0)}^b$ ($\times 10^9 L_1$)	$L_{\text{IR}}^{(*)}/(\tau_{\text{dust}})^c$ ($\times 10^{11} L_{\odot}$)(K)
00057+4021	0.97 ± 0.22	0.64 ± 0.14	1.43 ± 0.54	$\lesssim 0.23^d$	4.08 ± 0.62	2.9 (37)
00322-0840*	1.00 ± 0.35	0.58 ± 0.20			0.66 ± 0.17	0.55 (28)
00509+1225	0.84 ± 0.24	1.16 ± 0.40		0.35 ± 0.15	5.73 ± 1.18	0.96 (44)
01053-1746*		0.53 ± 0.14			12.2 ± 2.4	3.00 (33)
01077-1707*		0.32 ± 0.09			9.8 ± 2.0	3.00 (33)
01418+1651*		0.62 ± 0.17			2.5 ± 0.5	3.10 (45)
02071+3857	0.76 ± 0.16	0.70 ± 0.15			5.7 ± 0.46	0.78 (46)
0208+3725*		0.44 ± 0.12			1.5 ± 0.3	0.39 (50)
02114+0456*		0.84 ± 0.24			6.2 ± 1.2	1.64 (32)
02321-0900	1.10 ± 0.22	0.56 ± 0.14			4.0 ± 0.5	0.98 (61)
02401-0013*	1.00 ± 0.25	0.67 ± 0.16			1.22 ± 0.18	0.66 (74)
02483+4302	0.97 ± 0.22	0.44 ± 0.09		0.37 ± 0.13	3.6 ± 0.5	3.50 (36)
02512+1446*		0.22 ± 0.06			8.4 ± 1.7	1.85 (69)
03359+1523		0.18 ± 0.05			8.6 ± 1.3	2.05 (52)
04232+1436		1.09 ± 0.33		$\lesssim 0.28^d$	9.8 ± 2.0	7.45 (35)
05083+7936	0.72 ± 0.12	0.43 ± 0.19	1.46 ± 0.45	0.22 ± 0.07	11.53 ± 1.20	4.90 (52)
05189-2524	0.67 ± 0.15	0.59 ± 0.12	$\lesssim 0.90$	0.37 ± 0.14	3.91 ± 0.57	8.88 (60)
08030+5243	0.64 ± 0.16	0.36 ± 0.10			9.54 ± 1.90	5.96 (44)
08354+2555*	0.41 ± 0.08	0.42 ± 0.08			2.45 ± 0.30	2.01 (51)
08572+3915	0.98 ± 0.31			1.07 ± 0.44^e	1.60 ± 0.23	9.76 (52)
09126+4432	1.20 ± 0.26	0.53 ± 0.12			11.44 ± 1.62	2.22 (53)
09320+6134	1.23 ± 0.33	0.93 ± 0.24		$\lesssim 0.17^d$	4.82 ± 0.95	3.88 (40)
09586+1600*		0.74 ± 0.19			0.35 ± 0.07	0.25 (58)
10039-3338*		0.54 ± 0.16			3.36 ± 0.72	3.91 (52)
10035+4852	0.88 ± 0.24				9.11 ± 1.90	6.17 (48)
10173+0828		0.25 ± 0.07		$\lesssim 0.08^d$	6.0 ± 1.1	4.16 (48)
10190+1322	0.68 ± 0.18	0.68 ± 0.17			9.84 ± 1.85	5.81 (51)
10356+5345*	1.47 ± 0.42	1.21 ± 0.34			0.067 ± 0.013	0.27 (34)
10565+2448	1.06 ± 0.16	0.80 ± 0.12		0.18 ± 0.055	6.40 ± 0.65	6.45 (41)
11191+1200		0.54 ± 0.16		1.61 ± 0.58	0.50 ± 0.09	0.29 (41)
11231+1456*		0.32 ± 0.08			7.50 ± 1.03	2.00 (51)
11257+5850		0.83 ± 0.20	0.68 ± 0.21^f		2.72 ± 0.53	4.67 (47)
12001+0215*		0.25 ± 0.07			0.26 ± 0.053	0.070 (54)
12112+0305	0.90 ± 0.21	1.58 ± 0.35		0.29 ± 0.13^g	10.1 ± 1.2	12.1 (44)
12224-0624*		1.19 ± 0.55			0.67 ± 0.27	1.21 (37)
12243-0036*		0.84 ± 0.25			0.31 ± 0.07	0.66 (43)
12540+5708	0.89 ± 0.12	0.72 ± 0.13	0.80 ± 0.20	0.42 ± 0.13	7.0 ± 0.72	13.8 (44)
13001-2339*		0.63 ± 0.18			3.10 ± 0.62	1.81 (47)
13102+1251*		0.50 ± 0.15			0.52 ± 0.10	0.20 (50)
Arp 238*		0.30 ± 0.08			4.85 ± 0.97	4.00 ()
13183+3423	1.10 ± 0.19	0.74 ± 0.12		$\lesssim 0.09^d$	4.65 ± 0.40	2.21 (42)
13188+0036*		0.52 ± 0.15			2.28 ± 0.46	0.54 (34)
13229-2934	0.81 ± 0.13	0.57 ± 0.11			3.10 ± 0.39	0.68 (37)
13362+4831		0.58 ± 0.09			6.0 ± 0.70	2.09 (33)
13428+5608	0.82 ± 0.14	0.65 ± 0.13		0.17 ± 0.06	5.20 ± 0.60	8.37 (52)
13470+3530*		1.06 ± 0.30			1.47 ± 0.30	0.50 (31)
F13500+3141	0.75 ± 0.18	0.44 ± 0.13	1.01 ± 0.33	0.58 ± 0.20	4.63 ± 0.71	0.12 (57)
F13564+3741*		0.34 ± 0.10			1.67 ± 0.33	0.48 (31)
14003+3245*		1.63 ± 0.59			0.54 ± 0.16	0.50 (30)
14151+2705*		0.48 ± 0.14			4.65 ± 0.93	0.88 (52)
14178+4927*		0.88 ± 0.27			1.97 ± 0.43	0.48 (71)
14280+3126*		0.48 ± 0.12			1.16 ± 0.17	0.31 (52)
14348-1447	0.95 ± 0.21	0.71 ± 0.16			17.40 ± 2.5	14.1 (50)
15107+0724	1.26 ± 0.22	0.66 ± 0.11	0.58 ± 0.15	0.21 ± 0.06	0.87 ± 0.08	1.18 (33)
15163+4255*		0.35 ± 0.10			8.22 ± 1.65	4.10 (46)
15243+4150*		0.53 ± 0.18			0.18 ± 0.05	0.21 (57)
15322+1521*		0.82 ± 0.24			0.20 ± 0.04	0.13 (54)
15327+2340	0.67 ± 0.07	0.97 ± 0.14		0.21 ± 0.06	6.12 ± 0.53	10.0 (46)
15437+0234*		0.32 ± 0.10			1.61 ± 0.37	0.51 (52)
16104+5235*		0.76 ± 0.21			5.85 ± 1.17	1.87 (58)
16284+0411*		1.02 ± 0.32			1.67 ± 0.40	1.08 (40)

Table 7 – *continued* ^{12}CO line ratios and SF-powered IR luminosities

Name	r_{21}^a	r_{32}^a	r_{43}^a	r_{65}^a	$L'_{\text{CO}(1-0)}{}^b$ ($\times 10^9 L_1$)	$L_{\text{IR}}^{(*)} (T_{\text{dust}})^c$ ($\times 10^{11} L_{\odot}$)(K)
16504+0228	1.16 ± 0.22	1.10 ± 0.24		0.29 ± 0.08	8.41 ± 0.8	3.78 (53)
17132+5313	0.33 ± 0.07	0.23 ± 0.05			14.65 ± 2.1	1.26 (58)
17208-0014	1.08 ± 0.20	0.83 ± 0.16	0.90 ± 0.27	0.06 ± 0.025^h	13.10 ± 1.30	15.6 (46)
18425+6036*		0.68 ± 0.19			1.79 ± 0.36	0.44 (52)
19458+0944		1.00 ± 0.32			13.33 ± 2.80	10.0 (41)
20550+1656*		0.48 ± 0.13			7.10 ± 1.40	4.71 (42)
22491-1808	1.10 ± 0.32	1.88 ± 0.72^h			8.97 ± 1.63	13.0 (49)
23007+0836	0.75 ± 0.11	0.60 ± 0.10	0.83 ± 0.19	0.22 ± 0.06	3.48 ± 0.32	1.61 (42)
23365+3604	0.75 ± 0.17	0.82 ± 0.24	$\lesssim 0.78^d$	0.21 ± 0.09^h	7.30 ± 1.12	6.19 (61)

^aThe CO line ratios $r_{J+1J} = L'_{\text{CO}(J+1-J)} / L'_{\text{CO}(1-0)}$

^bThe CO 1–0 luminosity in units of $L_1 = K \text{ km s}^{-1} \text{ pc}^2$ (see Equation 6).

^cThe SF-powered part of L_{IR} and the associated dust temperature (see P10a for details).

^d3- σ upper limit.

^eCO J=6–5 flux from the NW nucleus where most of the CO emission is (Evans et al. 2002).

^fLikely higher as CO 4–3 is obtained from a partially completed map.

^gEstimated for the NE nucleus where 75% of CO(1–0) emission arises (Evans et al. 2002).

^hUncertain value, see footnotes of Tables 4,5.

Table 8. The CO/ ^{13}CO line ratios

Name	J=1–0 ^a	J=2–1 ^a
00057+4021		$\gtrsim 7^b$
00509+1225	8 ± 2	6 ± 2
01053-1746*	$\gtrsim 17^{b,c}$	
02071+3857	10 ± 2	12 ± 3
02401-0013*	14 ± 3	10 ± 3
02483+4302	$\gtrsim 13^b$	$\gtrsim 5^b$
03359+1523		12 ± 3
05083+7936	10 ± 3	10 ± 2
05189-2524		6 ± 2
08354+2555		$\gtrsim 18^{b,c}$
09126+4432		$\gtrsim 13^b$
09320+6134		18 ± 4
10035+4852		16 ± 5
10565+2448	15 ± 4	$\gtrsim 18^b$
11257+5850	27 ± 5^c	
12540+5708		47 ± 16
13183+3423		30 ± 7
13229-2934	26 ± 5	13 ± 2
13428+5608		7 ± 2
F13500+3141	$\gtrsim 4^b$	
14348-1447		12 ± 4
15107+0724	16 ± 4	24 ± 8
15327+2340	43 ± 10	17 ± 2
16504+0228	45 ± 14	53 ± 11
17208-0014		$\gtrsim 35^b$
23007+0836		15 ± 4
23365+3604		17 ± 5

^a $L'(\text{CO})/L'(^{13}\text{CO})$ line ratios.

^bRatio that corresponds to 3- σ upper limit on ^{13}CO flux.

^cRatio measured over a smaller area than that of total CO J=1–0 emitting region.

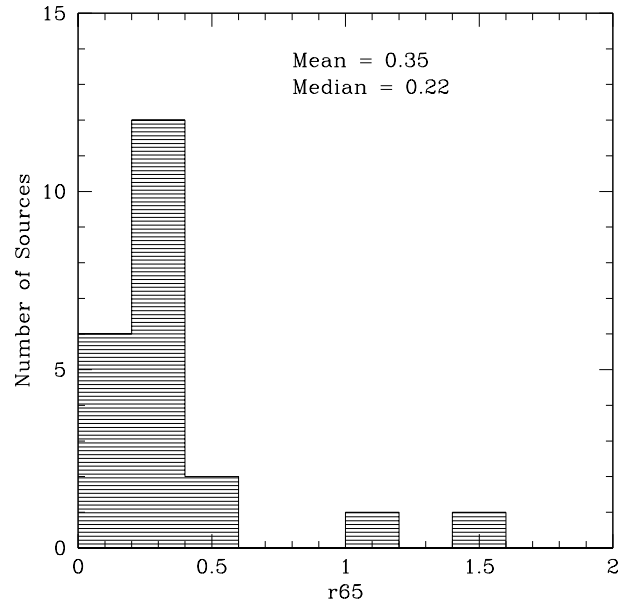


Figure 6. The distribution of the CO(6–5)/(1–0) brightness temperature ratios for the LIRGs in our sample. The optically luminous QSO PG 1119+120 has the highest excitation with $r_{65} \sim 1.6$. Some of the low ratios (≤ 0.3) may have been suppressed by a strong dust continuum becoming optically thick even at short submm wavelengths (see P10a).

(mostly) self-gravitating GMCs in the Galactic disk (and $K_{\text{vir}} \ll 1$ corresponding to dynamically unattainable gas motions). There is no theoretical upper limit for K_{vir} , and $K_{\text{vir}} \gg 1$ in regions where strong injection of turbulent energy occurs (e.g. in GMC/SNR interfaces). Indicatively, for average densities of $\sim (10^2 - 10^4) \text{ cm}^{-3}$ $K_{\text{vir}} = 20$ corresponds to $(dV/dR) \sim (5-50) \text{ km s}^{-1} \text{ pc}^{-1}$ (for $\alpha = 1.5$), encompassing the values observed in the highly turbulent gas of the Galactic Center (Dahmen et al. 1998; Oka et al. 1999), in pre-star-forming molecular clouds in the Galaxy

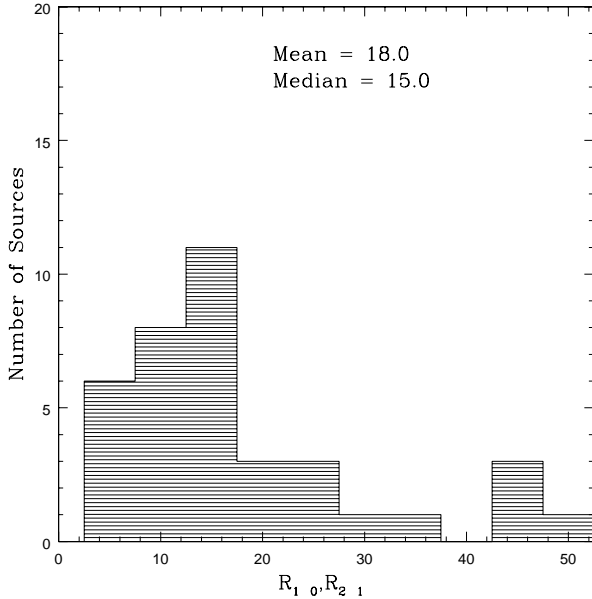


Figure 7. The joint distribution of the CO/¹³CO J=1–0, 2–1 line ratios for the LIRGs in our sample.

(Falgarone et al. 1998) and galactic SF nuclei where typically $(dV/dR) \sim (2-6) \text{ km s}^{-1} \text{ pc}^{-1}$ (Weiss et al. 2001). Furthermore we adopt $[\text{CO}/^{13}\text{CO}] = 50$ as appropriate for the environments in LIRGs (e.g. Henkel et al. 1993) and measured also for the Galactic disk in the Solar vicinity (Wilson & Penzias 1993), while we set $[\text{CO}/\text{H}_2] = 10^{-4}$ (needed for computing K_{vir} from Equation 12). Finally we note that some CO J=6–5 line luminosities may be diminished by significant dust optical depths even at short submm wavelengths (P10a,b), while in a few cases (e.g. Arp 193) they may be underestimated because of substantial pointing offsets. Thus we do not use them as constraints in our LVG modeling of the entire sample. Finally, we only made LVG models when $N \geq 3$ lines were available, except in the special cases where $r_{J+1,J} > 1$ that indicate quite unique high-excitation regions of the LVG parameter space.

In Figure 8 we show the T_{kin} , $T_{\text{r}}(1-0)$ (CO J=1–0 brightness temperature), $n(\text{H}_2)$, and K_{vir} distributions as derived from the LVG radiative transfer models, including the degenerate or poor solutions. A general $n(\text{H}_2)$ - T_{kin} degeneracy exists when $r_{J+1,J} < 1$ and ¹³CO lines are unavailable as constraints, with such ratios compatible with dense/cold and with diffuse/warm phases (e.g. for IRAS 14348-144: $10^4 \text{ cm}^{-3}/20 \text{ K}$ and $300 \text{ cm}^{-3}/150 \text{ K}$). These nevertheless typically have different K_{vir} , which can be used to discriminate between such disparate LVG solution ranges once ¹³CO lines become available. The few states with $n(\text{H}_2) \gtrsim 10^4 \text{ cm}^{-3}$ are associated with LIRGs where $r_{J+1,J} \geq 1$ (the high excitation tails in Figure 5), they also have $T_{\text{kin}} \gtrsim 100 \text{ K}$, and involve large molecular gas masses of $\sim (4-6) \times 10^9 M_{\odot}$. These extreme systems are studied in more detail in our final paper (Papadopoulos et al. 2012).

The wide K_{vir} distribution is a result of the large range of $R_{10,21}$ ratios (Figure 7), with average dynamical states having $K_{\text{vir}} \sim 0.7-2$ (\sim virial values) to $K_{\text{vir}} \gtrsim 20$ (strongly unbound states). This diversity is expected given that the galaxies in our sample include isolated disk-dominated systems (where GMCs are mostly self-gravitating) and strongly evolving mergers (where GMCs can be fully disrupted by tidal fields), and this has been noted from early studies of such systems (e.g. Aalto et al. 1995). The distri-

bution of the average brightness temperature of the CO J=1–0 line $T_{\text{r}}(1-0)$ is rather narrow, with an average of $\sim 16 \text{ K}$ and $\sigma(T_{\text{r}}) \sim 4 \text{ K}$ (for the distribution of the good, non-degenerate LVG solutions). The $\chi_{\text{g-d}} = T_{\text{kin}}/T_{\text{dust}}$ and $\chi_{\text{th}} = T_{\text{ex}}(3-2)/T_{\text{kin}}$ distributions (Figure 9) indicate how much “warmer” (or “colder”) a CO SLED is with respect to the SED of the concomitant dust reservoir, and the thermalization level of the J=3–2 transition.

For most LVG solutions $T_{\text{kin}}/T_{\text{dust}} \gtrsim 1$, which is expected since photoelectric, and even more so turbulent or CR heating of the ISM affect the dust much less. Only at very high densities ($\gtrsim 10^5 \text{ cm}^{-3}$ for Galactic ISM environments) thermal equilibrium between gas and dust is attained ($T_{\text{kin}} \sim T_{\text{dust}}$). Some large thermal decouplings ($\chi_{\text{g-d}} \gtrsim 3$) exist, with one of the highest found in the powerful radio galaxy 3C 293 where a strong jet-ISM interaction drives a “hot” CO SLED while its dust SED remains cold, reflecting Milky-Way levels of star formation (P10b). Thus turbulent heating (in this case AGN-driven) can heat *galaxy-sized* molecular gas reservoirs to high temperatures, even in the absence of strong SF-powered radiation fields, an important issue discussed further in section 7.1. The χ_{th} values range from very subthermal ($\sim 0.1-0.2$), to fully thermalized (~ 1) in the high-excitation ISM of some ULIRGs. Low χ_{th} values on the other hand are obtained mostly for a high temperature ($T_{\text{kin}} \sim (60-150) \text{ K}$), diffuse ($n(\text{H}_2) \sim (10^2-10^3) \text{ cm}^{-3}$) phase. This can be typical in turbulent GMC envelopes, and may even dominate the CO J=1–0, 2–1 line emission in ULIRGs (DS98), yet *it cannot contain much of their molecular gas mass*. Indeed in such galaxies with SF-powered IR luminosities of $L_{\text{IR}}^{(*)} \sim 10^{12} L_{\odot}$ (see P10b) the dense gas phase associated with SF sites will have a minimum mass of $M_{\text{SF}}(\text{H}_2) \sim L_{\text{IR}}^{(*)}/\epsilon_{\text{g,*}} \sim 4 \times 10^9 M_{\odot}$ (for an Eddington-limited SF efficiency of $\epsilon_{\text{g,*}} \sim 250 L_{\odot}/M_{\odot}$). This is already $\sim 2 \times M(\text{HI}+\text{H}_2)$ of gas-rich spirals (e.g. Young & Scoville 1991), the typical progenitors of ULIRGs (Sanders & Ishida 2004), thus leaving little room for any significant additional molecular gas mass in a diffuse phase in such systems. A very dense dense star-forming gas phase containing most of the molecular gas mass is indeed strongly suggested by HCN J=1–0 observations (Gao & Solomon 2004) and conclusively shown for individual ULIRGs using heavy rotor (e.g. HCN, CS) and ¹³CO lines (Papadopoulos et al. 2007; Greve et al. 2009).

6.1 Low-excitation CO SLEDs and the average ISM states

Only few “cold” CO SLEDs are found in our sample, indicated by the low excitation “tail” of CO line ratios with $r_{21} \leq 0.6$ and/or $r_{32} \leq 0.30$ (Figure 5). This is expected for what at the end is an IR-selected (and thus SFR-selected) galaxy sample, with the limitations of such samples in selecting large numbers of (cold-ISM)-dominated systems discussed thoroughly by Dunne et al. 2000. Furthermore, unlike the high excitation CO SLEDs that uniquely correspond to warm, dense (and often unbound) gas states, subthermally excited “cold” low-J CO SLEDs cannot be uniquely attributed to a quiescent ISM state. Indeed they could mark a cold ($\sim (10-20) \text{ K}$), self-gravitating ($K_{\text{vir}} \sim 1$) phase of moderate densities ($\sim 10^3 \text{ cm}^{-3}$), typical of SF-quiescent GMCs, but also a warmer ($\gtrsim 30 \text{ K}$), low-density ($\lesssim 10^3 \text{ cm}^{-3}$), and highly unbound gas phase ($K_{\text{vir}} \gg 1$) more typical of turbulent cloud “envelopes” or intercloud gas in ULIRGs (Aalto et al. 1995; Downes & Solomon 1998). This renders low-excitation CO J+1→J, J+1≤3 SLEDs *highly degenerate to the average state of the ISM in galaxies*. This is obvious in individual systems such as 3C 293 and Arp 220 where subthermal low-J CO lines give no hint about their massive and

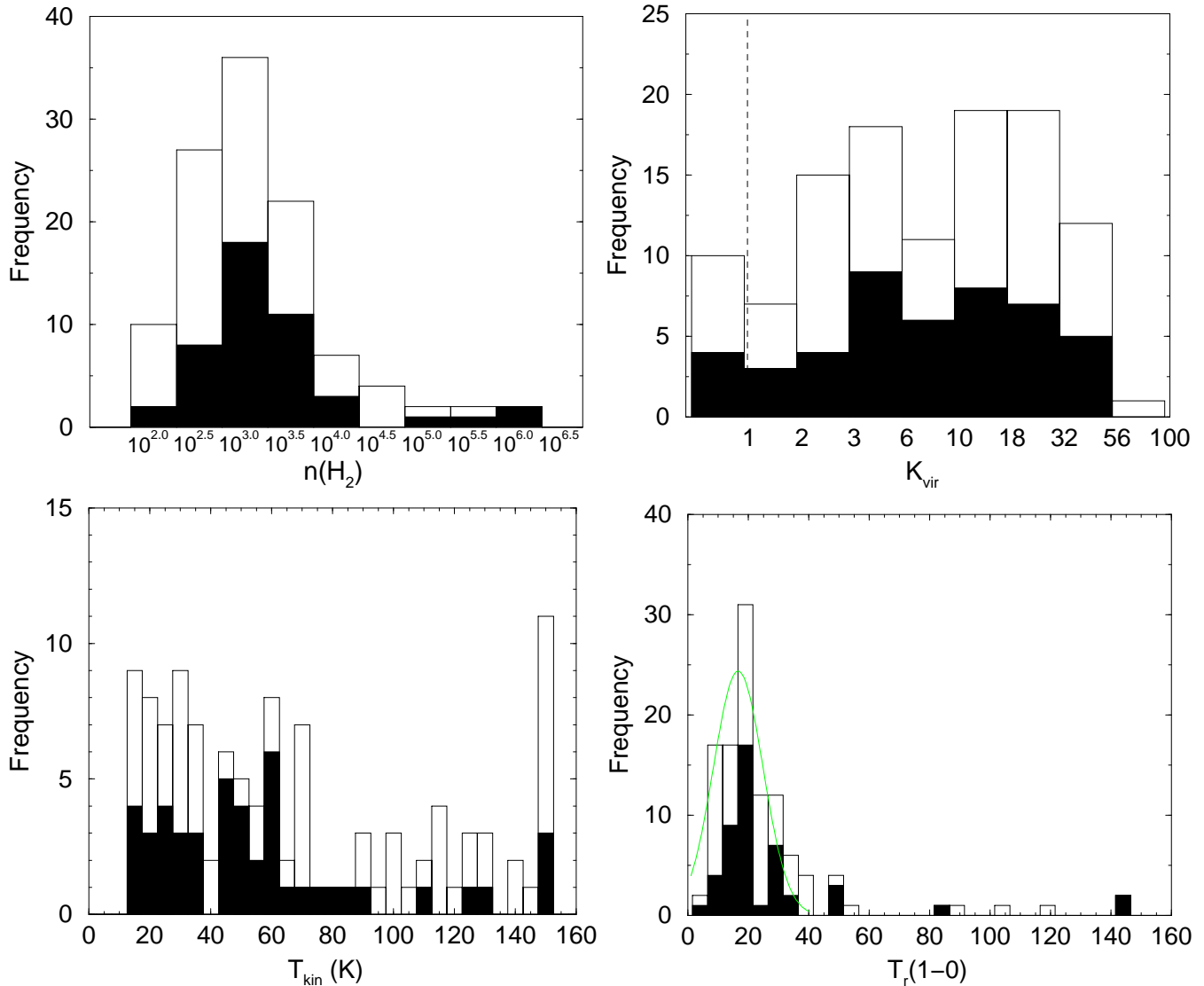


Figure 8. The $n(\text{H}_2)$, K_{vir} , T_{kin} , and $T_r(1-0)$ distributions obtained from one-phase LVG radiative transfer models of the CO lines of the LIRG sample. White bars: from all solutions, black bars: using only the best, non-degenerate LVG solutions obtained for each system (see section 6).

highly-excited gas reservoirs revealed only via CO $J+1 \rightarrow J$, $J+1 \geq 4$ or heavy rotor (e.g. HCN, CS) lines (Papadopoulos et al. 2008; Greve et al. 2009).

This degeneracy casts doubts on recent claims for Galactic-type ISM in distant gas-rich star-forming disks (Dannerbauer et al. 2009; Daddi et al. 2010) as current observations do not extend beyond CO $J=3-2$ where such degeneracies diminish (see section 7.2.1). Among the galaxies with low-excitation CO line ratios in our sample this was possible for only two LIRGs (IRAS 03359+1523 and IRAS 05189-2524) where available ^{13}CO line observations (see Table 8) played a key role in determining Galaxy-type ISM states as the most likely ones. Observations of ^{13}CO lines of distant systems like the BzK galaxies will soon become possible with ALMA and will be decisive in breaking the aforementioned degeneracies of low- J CO SLEDs with $R_{10,21} \sim 5-10$ corresponding to SF-quiescent Galactic-type ISM conditions while $R_{10,21} \gtrsim 15$ indicating vigorous star-forming and/or merger ISM environments.

7 CO SLEDs OF LIRGS: THEIR EXCITATION RANGE, AND POWER SOURCES

The range of normalized $L_{J+1,J}^{(n)} = L_{J+1,J} / L_{\text{IR}}$ CO SLEDs as determined from our study is shown in Figure 10. From this it becomes obvious that: a) beyond $J=3-2$ very large variations become possible, b) some global SLEDs are on par with those of the Orion SF “hot-spots”. The highest excitation SLED is AGN-driven (3C 293) followed by those for extreme starbursts (e.g. IRAS 17208-0014, IRAS 12112+0305). We must note that the large $L_{J+1,J}^{(n)}$ range, spanning $\sim 3-5$ orders of magnitude beyond $J=4-3$, reflects both the degeneracy of the one-phase radiative transfer models as well as the wide range of ISM excitation found in our sample. Recent Herschel/FTS observations of some of these (U)LIRGs fully determine this higher- J part of their CO SLEDs confirm this picture, and will be presented in a forthcoming paper. Finally from Figure 10 it is obvious that a positive K -correction for redshifted CO line emission from distant galaxies due to a rising $L_{J+1,J}^{(n)}$ with J -level (which makes possible the detection of very distant systems in high- J lines

by nearly countering luminosity-diminishing with distance) can be guaranteed only up to the J=3–2, 4–3 transitions.

7.1 Cosmic rays and turbulence: the dominant molecular gas heating mechanisms in ULIRGs?

What is to be made of those global CO SLEDs that are so highly excited that they are on par or even surpass those expected for the Orion SF “hot-spots”? Moreover, maintaining high temperatures ($T_{\text{kin}} \gtrsim 100$ K) for metal-rich gas with average densities $n(\text{H}_2) \gtrsim 10^5 \text{ cm}^{-3}$, as implied by some of these SLEDs, is difficult since cooling $\Lambda \propto [n(\text{H}_2)]^2$ (Lequeux 2005), and is thus $\sim 10^4$ - 10^6 times stronger than for average densities of molecular clouds ($\sim 10^2$ - 10^3 cm^{-3}). The galaxy-sized gas reservoirs ($\sim (2-5) \times 10^9 M_\odot$) involved make such highly-excited CO SLEDs even harder to maintain energetically since, for their high average densities, far-UV radiation fields will be reduced by factors of $\sim 10^4$ over distances of $\lesssim 0.1$ pc. The corresponding SF-powered PDRs will thus be very localized, involving only small fractions of a GMC’s mass, as demonstrated by the SF “hot-spots” in the Orion A, B clouds, while the same is expected for SNR-shocked regions (i.e. the “mechanical” counterpart of SF feedback).

Cosmic rays (CRs) and/or turbulence, already implicated as powerful heating sources of the molecular gas in Galactic Center (Yusef-Zadeh et al. 2007), and powering the high-excitation CO SLED of the starburst nucleus of NGC 253 (Bradford et al. 2003; Hailey-Dunsheath et al. 2008), can provide strong volumetric heating on the mass scales necessary to power the high-excitation CO SLEDs of ULIRGs. For CRs this has been recently demonstrated, with the large CR energy densities of $U_{\text{CR}} \sim [\text{few}] \times 10^3 U_{\text{CR, Gal}}$ expected in such galaxies penetrating much deeper into dense molecular regions than far-UV, optical and even IR photons and heating their mass up to ~ 100 K (Papadopoulos 2010). The very turbulent gas disks found in such galaxies (DS98) ($\sigma_v \sim (40-140) \text{ km s}^{-1}$ versus $\sigma_v \sim (5-6) \text{ km s}^{-1}$ for ordinary face-on spirals) and the dissipation of their supersonic velocity fields can considerably warm the molecular gas throughout their volume. Following Pan & Padoan 2009, the average turbulent heating rate is

$$\Gamma_{\text{turb}} = \mu m_{\text{H}} \langle \epsilon(\vec{x}, t) \rangle, \quad (13)$$

where $\mu=2.35$ is the mean molecular weight for molecular gas, n is the gas density, and $\langle \epsilon \rangle = \langle \epsilon(\vec{x}, t) \rangle = 1/2 (\sqrt{3} \sigma_v)^3 / L$ is the average turbulence dissipation rate per unit mass (assuming an isotropic velocity field). Using the σ_v -L (velocity dispersion)-(cloud size) relation

$$\sigma_v = \sigma_o \left(\frac{P_e}{P_o} \right)^{1/4} \left(\frac{L}{\text{pc}} \right)^\alpha \quad (14)$$

(Larson 1981), which is now well-established for the Galaxy with nearly constant $\sigma_o = 1.2 \text{ km s}^{-1}$ and power-law index $\alpha = 1/2$ (Heyer & Brunt 2004). The pressure-dependence of the normalization, with $P_o/k_B = 10^4 \text{ K cm}^{-3}$, can be derived from the virial theorem applied for clouds with boundary pressure P_e (Chiéze 1987; Elmegreen 1989). This pressure-dependence is very important as it predicts a higher normalization of the σ_v -L relation for high-pressure environments. This has actually been observed in the Galactic Center (Güsten & Phillip 2004) and astonishingly also in a molecular gas disk in a distant ULIRG at $z \sim 2.3$ (Swinbank et al. 2011). From Equations 13 and 14 after replacing the expression for $\langle \epsilon \rangle$, setting $\alpha = 1/2$, and substituting units we obtain

$$\Gamma_{\text{turb}} = 3.3 \times 10^{-27} n \sigma_{o,n} \left(\frac{P_e}{P_o} \right)^{3/4} L_{\text{pc}}^{1/2} \text{ erg cm}^{-3} \text{ s}^{-1} \quad (15)$$

where $\sigma_{o,n} = \sigma_o / (\text{km s}^{-1})$ and $L_{\text{pc}} = L / (\text{pc})$. On the other hand the (mainly) molecular line cooling for self-gravitating gas is well-approximated by the expression:

$$\Lambda_{\text{line}} = 1.9 \times 10^{-27} n \left(\frac{T_{\text{kin}}}{10\text{K}} \right)^3 \text{ erg cm}^{-3} \text{ s}^{-1} \quad (16)$$

(Papadopoulos 2010 and references therein), with most of it due to the CO SLEDs though other molecules (e.g. ^{13}CO) significantly contribute when $n \gtrsim 10^4 \text{ cm}^{-3}$ (Goldsmith 2001). Thus for thermal equilibrium: $\Gamma_{\text{turb}} = \Lambda_{\text{line}}$, we obtain

$$T_{\text{kin}} \sim 12 \sigma_{o,n}^{1/3} \left[\left(\frac{P_e/k_B}{10^4 \text{ K cm}^{-3}} \right)^{1/4} L_{\text{pc}}^{1/6} \right] \text{ K}. \quad (17)$$

Hence, for the typical pressures expected in the Galaxy and the midplane of ordinary spirals ($\sim 10^4 \text{ K cm}^{-3}$), turbulent heating can easily account for the temperatures of UV-shielded regions ($\sim (10-15) \text{ K}$), while insensitive to the spatial scales (L_{pc}) involved, and with a rather weak dependence on the pressure. However, for the dense gas-rich disks in ULIRGs the expected turbulent pressures can reach $\sim (1-3) \times 10^7 \text{ K cm}^{-3}$. Thus, for $\sigma_o = 1.2 \text{ km s}^{-1}$ and turbulent-driving at the largest scales $L_{\text{pc}} = 25-50$ (disk scale-heights in local ULIRGs, DS98) it would be $T_{\text{kin}} \sim (120-140) \text{ K}$. Atomic line cooling and gas-dust thermal interaction can lower these temperatures somewhat (e.g. Papadopoulos et al. 2011) which nevertheless remain high enough to power the extreme-excitation global CO SLEDs in these systems.

In reality both CR and turbulent heating will occur in the ISM of ULIRGs, powering high-excitation global CO SLEDs which would then be irreducible to ensembles of PDRs and/or SNR-shocked regions. This “irreducibility” has indeed been noted in the past for small molecular gas reservoirs ($\sim (10^6-10^7) M_\odot$) in the Galactic Center (Yusef-Zadeh et al. 2007) and the nucleus of NGC 253 (Bradford et al. 2003; Hailey-Dunsheath et al. 2008), yet in ULIRGs it will involve 3-4 orders of magnitude larger molecular gas masses. Unique observational signatures of such CR-dominated regions (CRDRs) or turbulently-heated regions (THRs) have been recently discussed in great detail (Papadopoulos 2010; Meijerink et al. 2011; Bayet et al. 2011) and most will be accessible to ALMA. Strong thermal decoupling of gas and dust with $T_{\text{kin}} \gg T_{\text{dust}}$, a common aspect of both heating mechanisms, can be revealed via high-resolution mm/submm imaging of dust continuum and line imaging of dense gas tracers dense gas (e.g. CS, HCN). High-J CO and ^{13}CO line (e.g. J=6–5, 7–6) imaging will be particularly valuable for distinguishing between the volumetrically heated CRDRs and THRs versus the surface-heated PDRs as those responsible for powering the observed CO SLEDs in (U)LIRGs (e.g. Hailey-Dunsheath et al. 2008).

7.2 CO SLEDs and X_{CO} values as SF mode indicators in galaxies

The low-efficiency (i.e. low $L_{\text{IR}}^*/M(\text{H}_2)$) and spatially distributed star formation in isolated gas-rich disks, and the high-efficiency one occurring in the compact merger-driven starbursts in ULIRGs can be thought as two distinct SF modes. The latter accounts for only 1% of the total SFR density in the local Universe, but could be dominant in the distant Universe (e.g. Hughes et al. 1998). However the discovery of very gas-rich disks ($f_{\text{gas}} \sim 0.5-0.6$) with extended low efficiency star-formation, and a space density 10-30 times higher than dusty mergers at high redshifts (Daddi et al. 2007), suggests

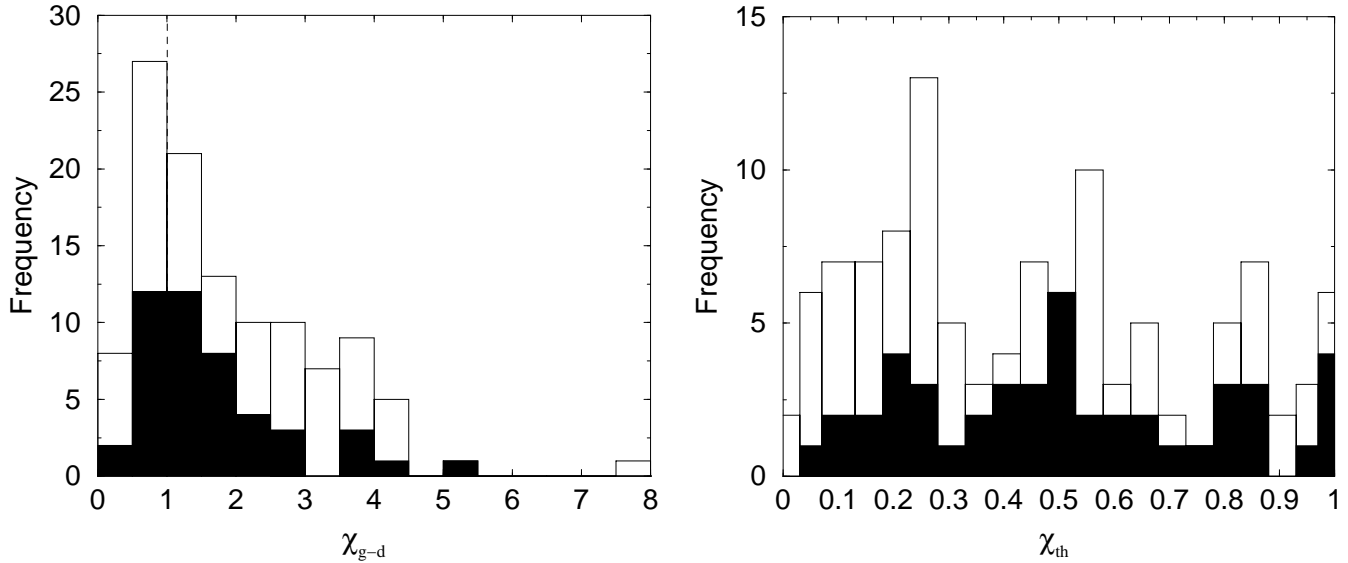


Figure 9. The $\chi_{g-d} = T_{\text{kin}}/T_{\text{dust}}$ and $\chi_{\text{th}} = T_{\text{ex}(3-2)}/T_{\text{kin}}$ distributions obtained from the one-phase LVG radiative transfer models (see section 6)

this mode as the prevalent one in the distant Universe. Recent studies of such disks reported a low CO(3-2)/(2-1) ratio and a near Galactic X_{co} factor, which were considered independent indicators of a disk-like low SFE mode (Dannerbauer et al. 2009; Daddi et al. 2010). Given the vast potential of molecular line observations in the upcoming era of ALMA, it is important to determine whether global CO SLEDs (by far the easiest to obtain for galaxies) and the corresponding X_{co} values are indeed reliable SF mode indicators.

The $r_{32/21}$ distribution obtained for our sample (Figure 11) makes obvious that the $r_{32/21}$ recently measured in a distant gas-rich disk (Dannerbauer et al. 2009) is within the range found for the vigorously star-forming LIRGs. Furthermore, as discussed previously, uniquely attributing MW-type ISM conditions to subthermal low-J CO ratios is problematic without additional constraints (e.g. ^{13}CO lines). Finally, a near-Galactic X_{co} factor *does not necessarily imply low-excitation SF-quietest ISM*. Indeed Galactic X_{co} values can be associated with both low-excitation SF-quietest ($T_{\text{b},1-0} \sim 10$ K, $n \sim 500 \text{ cm}^{-3}$) as well as dense warm gas ($T_{\text{b},1-0} \sim 60$ K, $n \sim 10^4 \text{ cm}^{-3}$) in star-forming sites since $X_{\text{co}} \propto \sqrt{n}/T_{\text{b},1-0}$. This is actually one of the main reasons for the robustness of X_{co} in estimating the mass of large molecular cloud ensembles which inadvertently encompass SF-quietest as well as SF gas in spiral disks (e.g. Young & Scoville 1991). Finally, any AGN-powering of high-J CO lines in otherwise SF-quietest galaxies, CR and/or turbulent heating, inject further uncertainties into any estimates of the dense/SF gas mass fraction $f_{\text{d}} = M(n > 10^5 \text{ cm}^{-3})/M_{\text{tot}}(\text{H}_2)$ (another potent measure of the SF mode) using CO SLEDs.

For a SF efficiency per dense molecular gas mass $\epsilon_{*,g} = L_{\text{IR}}^{(*)}/M_{\text{SF}}(\text{H}_2)$ that is a near-constant ($\sim (250-500) L_{\odot}/M_{\odot}$), and set by the physics underlying SF feedback onto the ISM (e.g. Scoville 2004; Andrews & Thompson 2011), the f_{d} becomes an equivalent and much better measure of SF modes with $f_{\text{d}}(\text{mergers/starbursts}) \sim (5-10) \times f_{\text{d}}(\text{disks/low-SF-efficiency})$ (e.g. Solomon et al. 1992; Gao & Solomon 2004; Wu et al. 2005). The latter assumes the HCN/CO J=1-0 ratio $r_{\text{HCN/CO}}$ as a good proxy, which is also more practical to obtain (low frequency observations) than high-J CO SLEDs. An extensive body of data in the local Uni-

verse allows both comparative studies of SF modes using “raw” $r_{\text{HCN/CO}}$ ratios, and their “calibration” in terms of actual f_{d} values (e.g. Papadopoulos et al. 2007; Gao & Solomon 2004). Sensitive CO and HCN J=1-0 and other types of molecular line observations that can discern SF modes of galaxies at high redshifts will be possible in the future with MeerKAT, the SKA, and ALMA (Geach & Papadopoulos 2012).

7.2.1 BzK galaxies as SF disks: well-excited CO SLEDs beyond $J=3-2?$

For the gas-rich disks of BzK galaxies at high redshifts: $L_{\text{IR}}^{(*)} \sim (1-4) \times 10^{12} L_{\odot}$, which corresponds to $M_{\text{SF}}(\text{H}_2) \sim (0.4-1.6) \times 10^{10} M_{\odot}$ of high-excitation gas (for $\epsilon_{*,g} = 250 M_{\odot}/L_{\odot}$). This is $\sim (5-13)\%$ of the $M_{\text{tot}}(\text{H}_2)$ reported for these systems (Daddi et al. 2010) with $\sim 10\%$ being average. Local spirals on the other hand have $M_{\text{SF}}(\text{H}_2)/M_{\text{tot}}(\text{H}_2) \sim (3-10)\%$ (e.g. IZw 1 in our sample), while in ULIRGs $M_{\text{SF}}(\text{H}_2)/M_{\text{total}}(\text{H}_2) \sim (20 \rightarrow 50)\%$ (e.g. Solomon et al. 1992; Gao & Solomon 2004; Greve et al. 2009). For a two-phase decomposition of molecular line emission (a SF-quietest and a SF-active phase) the global CO $\langle T_{\text{b}}(J+1-J) \rangle / \langle T_{\text{b}}(1-0) \rangle$ line ratio ($\langle \dots \rangle$ denote velocity/area averages) can be easily shown to be

$$r_{J+1,J} = r_{J+1,J}^{(h)} \left[\frac{1 + \frac{r_{J+1,J}^{(l)} X_{\text{co}}^{(h)}}{r_{J+1,J}^{(h)} X_{\text{co}}^{(l)}} \left(\frac{1-f_{\text{d}}}{f_{\text{d}}} \right)}{1 + \frac{X_{\text{co}}^{(h)}}{X_{\text{co}}^{(l)}} \left(\frac{1-f_{\text{d}}}{f_{\text{d}}} \right)} \right] \quad (18)$$

where (l) and (h) denote the quantities for the low and the high excitation phase. From COBE measurements (Fixsen et al. 1999) we obtain $r_{J+1,J}^{(l)} = 0.6, 0.28, 0.10, 0.046, \lesssim 0.028, \lesssim 0.017$ for $J+1=2,3,4,5,6,7$ (upper limits are 3σ) for the the inner Galaxy which we use, along with $X_{\text{co}}^{(l)} = 5 X_1$, to characterize the low-excitation, SF-quietest phase. For the high-excitation phase we use the CO (2-1)/(1-0) ($\sim 1.2-1.3$) and CO/ ^{13}CO J=2-1 (~ 10) ratios obtained for the SF “hot-spots” of Orion A and B (Sakamoto et al. 1994) as constraints on a LVG one-phase model. The densest and warmest phase compatible with them ($T_{\text{kin}} = (125-150)$ K, $n \sim 3 \times 10^5 \text{ cm}^{-3}$, and $K_{\text{vir}} = 7$) yields a CO SLED template with

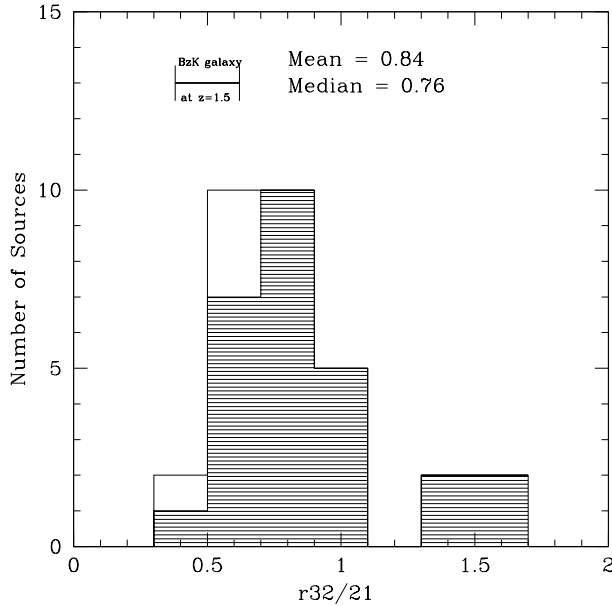


Figure 11. The CO (3-2)/(2-1) brightness temperature distribution for our sample (shaded area: sources with CO source size $\leq 14''$), with the range corresponding to a measured value for a gas-rich disk in a BzK galaxy at $z \sim 1.5$ (Dannerbauer et al. 2009).

$r_{J+1,J}^{(h)} = 1.35, 1.33, 1.30, 1.27, 1.25, 1.22$ for $J+1=2,3,4,5,6,7$, and a corresponding $X_{\text{CO}}^{(h)} = 2.2 X_{\text{I}}$. Then Equation 18 yields $r_{J+1,J} = 0.75, 0.49, 0.34, 0.29, 0.27, 0.26$ for $J+1=2,3,4,5,6,7$. The r_{65} and r_{76} values assume the upper limits for $r_{65}^{(l)}$ and $r_{76}^{(l)}$, while setting the latter to zero yields $r_{65}^{(l)} = 0.25$ and $r_{76}^{(l)} = 0.24$ as minimum values.

Figure 12 shows the CO SLED for a fiducial gas-rich disk with 10% of its molecular gas mass in the SF phase along with the one for the inner Galaxy. For typical measurement uncertainties of $\sigma(r)/r \sim 0.25-0.30$, only ratios $r_{J+1,J}$ with $J+1 \geq 4$ markedly deviate from a Galactic CO SLED while lower-J lines will remain compatible with it. It is thus obvious that for the average SF gas mass fraction in BzK galaxies *their CO SLEDs will be significantly more excited from that of the Galaxy beyond $J=3-2$* . Future observations of higher-J CO lines in such systems are necessary to verify this.

8 CONCLUSIONS, AND SOME IMPORTANT OPEN QUESTIONS

We present multi-J ^{12}CO and ^{13}CO line data of total line luminosities for a sample of IR-luminous galaxies ($N=36$) which includes the most intense starbursts known in the local Universe. We then conducted a detailed literature search for all other IR-luminous galaxies with available total CO line luminosities up to at least $J=3-2$, the transition where the dense and warm star-forming gas phase starts dominating the CO SLEDs. The final sample contains 70 galaxies with IR luminosities of $L_{\text{IR}}^{(*)} \sim (10^{10}-2 \times 10^{12}) L_{\odot}$, morphologies ranging from isolated disks to strong mergers, and is an excellent resource for follow-up molecular line observations (e.g. HCN, CS, HCO^+) and mm/submm imaging of the CO or other molecular SLEDs with ALMA ($\sim 2/3$ of the sample is accessible from Llano Chajnantor). In the present study it was used to obtain a better overall picture of the average physical conditions of the molecular gas in star-forming galaxies, our findings are as follows:

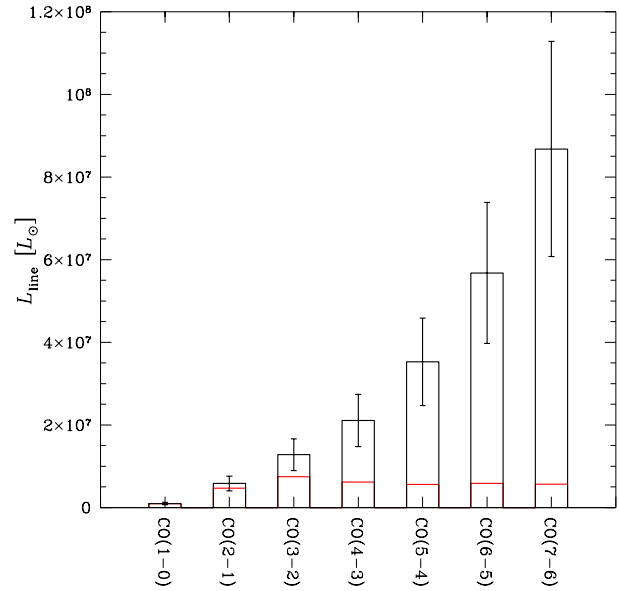


Figure 12. The CO SLED of a gas-rich disk with 10% of its molecular gas mass in a SF gas phase (typical for BzK galaxies) with the typical 30% dispersion expected from measurement errors (black line). The CO SLED of the inner Galaxy is marked by the red lines (see 7.2.1).

(i) There is a surprisingly wide range of CO line excitation, from subthermally-excited low-J transitions, to thermalized ones up to $J=4-3, 6-5$. A positive K-correction is assured only up to the $J=3-2, 4-3$ lines, beyond which large variations of the emergent IR-normalized ($L_{J+1,J}/L_{\text{IR}}^{(*)}$) line luminosities are expected.

(ii) The highly excited global CO SLEDs are found solely in starburst galaxies with $L_{\text{IR}} > 10^{11} L_{\odot}$, with the exception of two found in galaxies with low or moderate star formation but hosting powerful AGN. Such SLEDs imply tremendous amounts of molecular gas mass ($\sim (\text{few}) \times 10^9 M_{\odot}$) in a dense ($\gtrsim 10^4 \text{ cm}^{-3}$) and very warm ($T_{\text{kin}} \gtrsim 100 \text{ K}$) state.

(iii) The high densities and temperatures, as well as the strongly unbound motions ($K_{\text{vir}} \gg 1$) often found for the molecular gas of ULIRGs underlie global CO SLEDs which can remain well-excited and become partly optically thin up to high-J transitions. In the Galaxy such SLEDs are found only in strongly irradiated gas near HII regions and shocked gas in SNR-molecular cloud interfaces and involving only $\sim (1-5)\%$ of the mass of individual Giant Molecular Clouds. In some ULIRGs of our sample the warm and dense gas phase can contain $\gtrsim 50\%$ of their total molecular gas mass.

(iv) Highly supersonic turbulence and high CR energy densities, both permeating the ISM of ULIRGs, can volumetrically heat large amounts of dense gas to high temperatures, and easily account for their observed highly excited SLEDs. In the compact, and heavily dust-enshrouded ISM environments of ULIRGs such heating mechanisms may actually dominate over the classical mechanism via the far-UV/optical radiation fields and the photoelectric effect. The resulting highly excited global CO SLEDs will be irreducible to ensemble averages of Photon-dominated Regions (PDRs), an exciting possibility that will be further explored with Herschel observations of the complete J-ladder above $J=4-3$ for several ULIRGs in our sample (Key project HerCULES).

(v) As expected for a sample of IR-selected (and thus vigorously star-forming) galaxies, only few low-excitation CO SLEDs

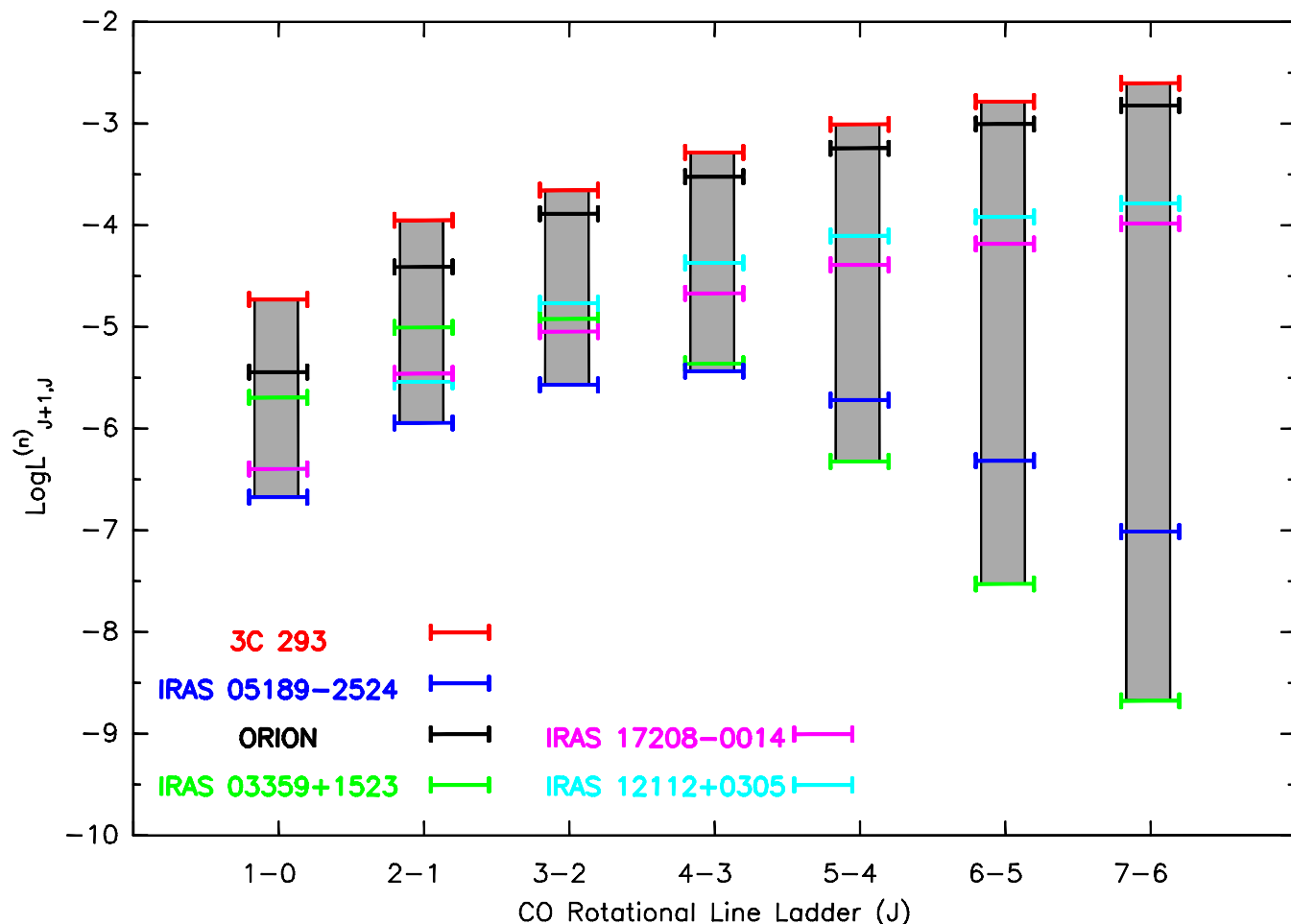


Figure 10. The range of the normalized $L_{J+1,J}^{(n)} = L_{J+1,J} / L_{\text{IR}}^{(*)}$ CO SLEDs of the sample, along with a few key systems (lines beyond $J=4-3$ are interpolated using one-phase LVG models).

are found. For only two of them a cold and gravitationally bound phase with moderate/low densities (typical of SF-quiescent molecular gas) emerges as the most likely ISM state, while the rest of the “cold” CO SLEDs may still belong to starburst systems. Only ^{13}CO and/or CO $J+1 \rightarrow J$, $J+1 > 3$ lines can reduce this well-known degeneracy, and as a result the low- J part of global CO SLEDs ($J=1-0$, $2-1$, $3-2$) cannot be a unique indicator of the SF mode (i.e. merger-driven compact starburst versus isolated-disk low-efficiency star formation) in galaxies.

(vi) The gas-rich disks recently discovered at high redshifts are examples of galaxies whose “cold” low- J CO SLEDs have been used to indicate Galactic-type low-excitation ISM, yet higher- J ($J=4-3$ and higher) CO transitions are expected to be highly-excited and indicative of much more vigorous star formation environments than those found in local spirals.

8.1 Important open questions

If strong turbulence and/or high CR energy densities are responsible for the large amounts of very warm and dense gas found in some ULIRGs, they will also *change the initial conditions of star formation in such galaxies*, set deep inside UV-shielded dense gas regions. The new conditions can lead towards a top-heavy stellar Initial Mass Function (IMF) (Hocuk & Spaans 2010; Papadopoulos et al. 2011) with ground-breaking implications for the interpre-

tation of IR/optical SEDs and H II region optical-IR lines of such systems in terms of star formation rates. Nevertheless the current data, while strongly suggestive of different dominant heating mechanisms operating deep inside dense molecular clouds in ULIRGs, they cannot determine their state in detail. Recent work (Bayet et al. 2011; Meijerink et al. 2011) demonstrates this to be possible using the high-frequency coverage provided by Herschel, and the increased sensitivity in the mm/submm regime soon to be provided by ALMA.

Finally, the wide range of average ISM conditions found in star-forming IR-luminous galaxies will strongly impact the so-called X_{CO} factor. Indeed it becomes rather hard to argue in favor of one convenient, ULIRG-appropriate, X_{CO} factor given the diversity of CO SLEDs found even within the ULIRG class. The strong supersonic turbulence alone will “re-settle” large portions of molecular gas mass in such systems towards high density phases. These would be traceable only via high- J CO and heavy rotor (e.g. HCN, CS) transitions while low- J CO lines will be dominated by a warm, diffuse and unbound gas phase that contains little mass and has misleadingly “cold” low CO ratios. These issues are now addressed in detail in Paper II (Papadopoulos et al. 2012).

ACKNOWLEDGMENTS

YG's research is partially supported by China NSF grants No 11173059, 10833006 and 10621303. The project was funded also by the John S. Latsis Public Benefit Foundation. The sole responsibility for the content lies with its authors. We would like to thank the referee Jonathan Braine for his thorough reading of a rather extensive manuscript and comments that improved the clarity of this work. PPP would like to also thank Zhi-Yu Zhang for help with Figure 10, and Yiping Ao for his diligent reading and commenting on the plots and our results. Finally a decade-long work of this scope would have been impossible without the continuous and expert support provided from all the people at the Joint Astronomy Center in Hilo, Hawaii, that made the JCMT the success story it has been over two two and a half decades of its operation.

REFERENCES

- Aalto S., Johansson L. E. B., Booth R. S., & Black J. H. 1991, *A&A*, 249, 323
- Aalto S., Booth R. S., Black J. M., & Johansson L. E. B. 1995 *A&A*, 300, 369
- Aalto S., Garcia-Burillo S., Muller S. et al. 2012, *A&A*, 537, 44
- Albrecht M., Krügel E., & Chini R. 2007, *A&A*, 462, 575
- Allen R. J., Le Bourlot J., Lequeux J., Pineau des Forêts G., Roueff E. 1995, *ApJ*, 444, 157
- Andrews B. H., & Thompson T. A. 2011, *ApJ*, 727, 97
- Arikawa Y., Tatematsu K., Sekimoto Y., & Takahashi T. 1999, *PASJ*, 51, L7
- Barvainis R., Alloin D., & Antonucci R. 1989, *ApJ*, 337, L69
- Balick B., & Heckman T. M. 1981, *A&A*, 96, 271
- Bayet E., Gerin M., Phillips T. G., & Contursi A. 2006, *A&A*, 460, 467
- Bayet E., Williams D. A., Hartquist T. W., Viti S. 2011, *MNRAS*, 414, 1583
- Bolato A. D. Leroy A., Israel F. P. & Jackson J. M. 2003, *ApJ*, 595, 167
- Bradford C. M., Nikola T., Stacey G. J. et al. 2003, *ApJ*, 586, 891
- Braine J., & Combes F. 1992, *A&A*, 264, 433
- Braine J., Combes F., Casoli F., et al. 1993, *A&AS*, 97, 887
- Bryant P. M., & Scoville N. Z. 1996, *ApJ*, 457, 678
- Bryant P. M., & Scoville N. Z. 1999, *AJ*, 117, 2632
- Bussmann R. S., Narayanan D., Shirley Y. L., Juneau S., Wu J., Solomon P. M., Vanden Bout P. A., Moustakas J., & Walker C. K. 2008, *ApJ*, 681, L73
- Carico D. P., Sanders D. B., Soifer B. T., Matthews K., & Neugebauer G. 1990, *AJ*, 100, 70
- Casoli F., Durpaz C., & Combes F. 1992, *A&A*, 264, 55
- Chiéze J. P. 1987, *A&A*, 171, 225
- Condon J. J., Helou G., Sanders D. B., & Soifer B. T. 1990, *ApJS*, 73, 359
- Condon J. J., Helou G., Sanders D. B., & Soifer B. T. 1996, *ApJS*, 103, 81
- Crawford T., Marr J., Partridge B., & Strauss M. 1996, *ApJ*, 460, 225
- Daddi E., et al. 2007, *ApJ*, 670, 156
- Daddi E., 2009, private communication
- Daddi E., Bournaud F., Walter F., et al. 2010, *ApJ*, 713, 686
- Dahmen G., Hüttemeister S., Wilson T. L., & Mauersberger R. 1998, *A&A*, 331, 959
- Dannerbauer H., Daddi E., Riechers, D. et al. 2009, 698, L178
- Dasyra K., et al. 2006, *ApJ*, 638, 745
- Devereux N., Taniguchi Y., Sanders D. B., Nakai N., & Young J. S. 1994, *AJ*, 107, 2006
- Dopita M. A., Groves B. A., Fischera J. et al. 2005, *ApJ*, 619, 755
- Downes D., Solomon, P. M. & Radford, S. J. E. 1993, *ApJ*, 414, L13
- Downes D., Solomon, P. M. 1998, *ApJ*, 507, 615
- Dumke M., Nietten Ch., Thuma G., Wielebinski R., & Walsh W. 2001, *A&A*, 373, 853
- Dunne L., Eales S., Edmunds M., Ivison R., Alexander P., & Clements D. L. 2000, *MNRAS*, 315, 115
- Eckart A., van der Werf P., Hofmann R., & Harris I. 1994, *ApJ*, 424, 627
- Elmegreen B. G. 1989, *ApJ*, 338, 178
- Evans A. S., Sanders D. B., Surace J. A., & Mazzarella J. M. 1999, *ApJ*, 511, 730
- Evans A. S. Surace J. A., & Mazzarella J. M. 2000, *ApJ*, 529, L85
- Evans A. S., Frayer D. T., Surace J. A., & Sanders D. B. 2001, *AJ*, 121, 3286
- Evans A. S., Mazzarella J. M., Surace J. A., & Sanders D. B. 2002, *ApJ*, 580, 749
- Evans A. S., Mazzarella J. M., Surace J. A., et al. 2005, *ApJS*, 159, 197
- Falgarone E., Panis J.-F., Heithausen A., Stutzki J., Puget J.-L., & Bensch F., 1998, *A&A*, 331, 669
- Fixsen D. J., Bennett C. L., & Mather J. C., 1999, *ApJ*, 526, 207
- Gao Y., & Solomon P. M. 2004, *ApJ*, 606, 271
- Geach J. E. & Papadopoulos P. P. 2012, *ApJ*, (submitted)
- Genzel R., Lutz D., Sturm E., et al. 1998, *ApJ*, 498, 579
- Genzel R., Tacconi L. J., Rigopoulou D., Lutz D., & Tecza M. 2001, *ApJ*, 563, 527
- Goldsmith P. F. 2001, *ApJ*, 557, 736
- Güsten R., Serabyn E., Kasemann C., et al., 1993, *ApJ* 402, 537
- Güsten R., Philipp S. D. 2004, in *The Dense Interstellar Medium in Galaxies* Proceedings of the 4th Cologne-Bonn-Zermatt Symposium, Zermatt, Switzerland, S.Pfalzner, C. Kramer, C. Staubmeier, and A. Heithausen (Eds) Springer, Vol. 91. p. 253
- Greve T. R., Bertoldi F., Smail I., et al. 2005, *MNRAS*, 359, 1165
- Greve T. R., Papadopoulos P. P., Gao Y., & Radford S. J. E. 2009, *ApJ*, 692, 1432
- Graciá-Carpio J., Planesas P., & Colina L. 2007, *A&A*, 468, L67
- Güsten R., Serabyn E., Kasemann C., et al. 1996, *ApJ*, 402, 537
- Hailey-Dunsheath S., Nikola T., Stacey G. J., Oberst T. E., Parshley S. C., Bradford C. M., Ade P. A. R., & Tucker C. E. 2008, *ApJ*, 689, L109
- Henkel C., Mauersberger R., Wiklind T., Hüttemeister S., Lemme C., & Millar T. J. 1993, *A&A*, 268, L17
- Heyer M. H., & Brunt C. M. 2004, *ApJ*, 615, L45
- Hocuk S., & Spaans M. 2010, *A&A*, 510, 110
- Horellou C., Casoli F., Combes F., & Durpaz C. 1995, *A&A*, 298, 743
- Hughes D., Serjeant S., Dunlop J. et al. 1998, *Nature*, 394, 241
- Iono D., Ho P. T., Yun M. S., Matsushita S., Peck B. A., & Sakamoto K. 2004, *ApJ*, 616, L63
- Iono D., Wilson C. D., Takakuwa S. et al. 2007, *ApJ*, 659, 283
- Iono D., Wilson C. D., Yun M. S. et al. 2009, *ApJ*, 695, 1537
- Ivison R. J., Papadopoulos P. P., Smail I. et al. 2011, *MNRAS*, 412, 1913
- Krügel E., Steppe H., & Chini R. 1990, *A&A*, 229, 17
- Knapp G. R. Phillips T. G., Huggins P. J. Leighton R. B., Wannier P. G. 1980, *ApJ*, 240, 60
- Kutner M. L., & Ulich B. L. 1981, *ApJ*, 250, 341
- Larson R. B. 1981, *MNRAS*, 194, 809
- Leech J., Isaak K., Papadopoulos P. P., Gao Y., & Davies G. R. 2010, *MNRAS*, 406, 1364
- Lequeux J. 2005, *The Interstellar Medium*, *A&A Library*, Springer-Verlag pg. 197
- Lisenfeld U., Isaak K. G., & Hills R. 2000, *MNRAS*, 312, 433
- Loinard L., Allen R. J., & Lequeux J. 1995, *A&A*, 301, L68
- Krips M., Neri R., Graciá-Burillo S., Martin S., Combes F., Graciá-Carpio J., & Eckart A. 2008, *ApJ*, 677, 262
- Mao R. Q., Henkel C., Schulz A., et al. 2000, *A&A*, 358, 433
- Mao R. Q., Schulz A., Henkel C., Mauersberger R., Muders D., & Dinh-V-Trung 2011, *ApJ*, 724, 1336
- Matsushita S., Sakamoto K., Kuo C.-Y., et al. 2004, *ApJ*, 616, L55
- Mauersberger R., Henkel C., Walsh W., & Schulz A. 1999, *A&A*, 341, 256
- Mazzarella J. M., Graham J. R. Sanders D. B., & Djorgovski S. 1993, *ApJ*, 409, 170
- Meier D. S., Turner J. L., & Crosthwaite L. P. & Beck S. C. 2001, *AJ*, 121, 740
- Meijerink R., & Spaans M. 2005, *A&A*, 436, 397
- Meijerink R., Spaans M., & Israel F. P. 2006, *ApJ*, 650, L103
- Meijerink R., Spaans M., Loenen A. F., van der Werf P. P. 2011, *A&A*, 525, 119
- Meixner M., Puchalsky R., Blitz L., Wright M., & Heckman T. 1990, *ApJ*, 354, 158

- Mirabel I. F., Booth R. S., Johansson L. E. B., Garay G., & Sanders D. B. 1990, *A&A*, 236, 327
- Mortier A., Isaak K., Gao Y., Leech J. 2011, *MNRAS* (submitted)
- Murphy T. W. Jr., Armus L., Matthews K., Soifer B. T., Mazzarella J. M., Shupe D. L. 1996, *AJ*, 111, 1025
- Narayanan D., Groppi C. E., Kulesa C. A., & Walker C. K. 2005, *ApJ*, 630, 269
- Nieten Ch., Dumke M., Beck R., & Wielebinski R. 1999, *A&A*, 347, L5
- Olofsson H., Rydbeck G. 1984, *A&A*, 136, 17
- Oka T., Hasegawa T., Sato F., Tsuboi M., & Miyazaki A. 1998, *ApJS*, 118, 455
- Oka T., White G. J., Hasegawa T., Sato F., Tsuboi M., & Miyazaki A. 1999, *ApJ*, 515, 249
- Pan L., & Padoan P. 2009, *ApJ*, 692, 594
- Papadopoulos P. P. & Seaquist E. R. 1999, *ApJ*, 516, 114
- Papadopoulos P. P. & Allen M. L. 2000, *ApJ*, 537, 631
- Papadopoulos P. P. & Ivison R. J. 2002, *ApJ*, 564, L9
- Papadopoulos P. P. 2007, *ApJ*, 656, 792
- Papadopoulos P. P., Isaak K. G., & van der Werf P. P. 2007, *ApJ*, 668, 815
- Papadopoulos P. P., Isaak K. G., & van der Werf P. P. 2010a, *ApJ*, 711, 757
- Papadopoulos P. P., van der Werf P. P., Isaak K. G., & Xilouris E. M. 2010b, *ApJ*, 715, 775
- Papadopoulos P. P. 2010, *ApJ*, 720, 226
- Papadopoulos P. P., Thi, W.-F., Miniati F., & Serena V. 2011, *MNRAS*, 414, 1705
- Papadopoulos P. P., van der Werf P. P., Xilouris E., Isaak K. G., & Gao Y. 2012 (Paper II), *ApJ*, (in press, arXiv:1202.1803)
- Petitpas G. R., & Wilson C. D. 1998, *ApJ*, 503, 219
- Planesas P., Mirabel I. F., & Sanders D. B. 1991, *ApJ*, 370, 172
- Polk K. S., Knapp G. R., Stark A. A., & Wilson R. W. 1988, *ApJ*, 332, 432
- Rowan-Robinson M. 2001, *New Astronomy Reviews*, Vol. 45, 631
- Sakamoto S., Hayashi M., Hasegawa T., Handa T., & Oka T. 1994, *ApJ*, 425, 641
- Sakamoto S. PhD Thesis, 1994, University of Tokyo, PASP 106, 1112
- Sakamoto K., Wang J., Wiedner M., et al. 2008, *ApJ*, 684, 957
- Sanders D. B., Scoville N. Z., Young J. S., Soifer B. T., Schloerb F. P., Rice W. L., & Danielson G. E. 1986, *ApJ*, 305, L45
- Sanders D. B., Scoville N. Z., Sargent A. I., & Soifer B. T. 1988a, *ApJ*, 324, L55
- Sanders D. B., Soifer B. T., Elias J. H. et al. 1988b, *ApJ*, 325, 74
- Sanders D. B., Soifer B. T., Elias J. H., Neugebauer G., & Matthews K. 1988c, *ApJ*, 328, L35
- Sanders D. B., Scoville N. Z., & Soifer B. T. 1991, *ApJ*, 370, 15 8
- Sanders D. B., & Mirabel I. F. 1996, *ARA&A*, 34, 749
- Sanders D. B. Mazzarella J. M., Kim D.-C., Surace J. A., & Soifer B. T. 2003, *AJ*, 126, 1607
- Sanders D. B., & Ishida C. M. 2004, in *The Neutral ISM in Starburst Galaxies*, eds. S. Aalto, S. Hüttemeister, & A. Pedlar, ASP Conference Series 320, p. 230
- Schinnerer E., Eckart A., & Tacconi L. J. 1998, 500, 147
- Scoville N. Z., Sanders D. B., Sargent A. I., Soifer B. T., & Tinney C. G. 1989, *ApJ*, 345, L25
- Scoville N. Z. 2004, Evans A. S., Thompson R., Rieke M., Hines D. C., F. J., Dinshaw N., Surace J. A., & Armus L. 2000, *AJ*, 119, 991
- Scoville N. Z. 2004, in *The Neutral ISM in Starburst Galaxies*, eds. S. Aalto, S. Hüttemeister, & A. Pedlar, ASP Conference Series 320, p. 253
- Schleicher D. R. G., Spaans M., & Klessen R. S. 2010, *A&A*, 513, 7
- Seta M., Hasegawa T., Dame T M. et al. 1998, *ApJ*, 505, 286
- Shirley Y. L., Evans N. J. II., Young K. E., Knez C., & Jaffe D. T. 2003, *ApJS*, 149, 375
- Soifer B. T., Sanders D. B., Madore B. F., et al. 1987, *ApJ*, 320, 238
- Soifer B. T., Bohemer L., Neugebauer G., & Sanders D. B. 1989, *AJ*, 98, 766
- Soifer B. T., & Neugebauer G. 1991, *AJ*, 101, 354
- Solomon P. M., Rivolo A. R., Barrett J. W., & Yahil A. 1987, *ApJ*, 319, 730
- Solomon P. M., Radford S.J.E., & Downes D. 1990, *ApJ*, 348, L53
- Solomon P. M., Downes D., & Radford S.J.E. 1992, *ApJ*, 387, L55
- Solomon P. M., Downes D., Radford S.J.E., & Barrett J. W. 1997, *ApJ*, 478, 144
- Solomon P. M., & Vanden Bout P. A., 2005, *ARA&A*, 43, 677
- Smail I., Ivison R. J., & Blain A. W. 1997, *ApJ*, 490, L5
- Staguhn J. G., Schinnerer E., Eckart A., & Scharwächter J. 2004, *ApJ*, 609, 85
- Surace J. A., Sanders D. B., Vacca W. D., Veilleux S., & Mazzarella J. M. 1998, *ApJ*, 492, 116
- Surace J. A., Sanders D. B., & Evans A. S. 2000, *ApJ*, 529, 179
- Tacconi L. J., & Genzel R. 1996 in *Science with Large Millimetre Arrays* Proceedings of the ESO-IRAM-NFRA-Onsala Workshop, Garching, Germany, Peter A. Shaver (Ed.) Springer-Verlag, p.125
- Tacconi L. J., Genzel R., Lutz D., et al. 2002, *ApJ*, 580, 73
- Tacconi L. J., Neri R., Chapman S. C., et al. 2006, *ApJ*, 640, 228
- Thomas H. C., Clemens M. S., Alexander P., Green D. A., Eales S., & Dunne L. 2001, ASP Conference Proceedings, Vol. 240, pg. 224
- Thompson T. A., Quataert E., & Murray N. 2005, *ApJ*, 630, 167
- Thompson T. A. 2009, *Astronomical Society of the Pacific Conference Series*, 408, 128
- Tinney C. G., Scoville N. Z., Sanders D. B., & Soifer B. T. 1990, *ApJ*, 362, 473
- van der Werf P. P. Isaak K. G., Meijerink R. et al. 2010, *A&A*, 518, L42
- Veilleux S., Kim D.-C., & Sanders D. B. 2002, *ApJS*, 143, 315
- Wall W. F., Jaffe D. T., Bash F. N., Israel F. P., Maloney P. R., & Baas F. 1993, *ApJ*, 414, 98
- Walter F. et al. 2003, *Nature*, 424, 406
- Wang Z., Scoville N. Z., & Sanders D. B. 1991, *ApJ*, 368, 112
- Weiss A., Neininger N., Hüttemeister S., & Klein U. 2001, *A&A*, 365, 571
- Weiss A., Walter F., & Scoville N. Z. 2004, in *The Neutral ISM in Starburst Galaxies*, eds. S. Aalto, S. Hüttemeister, & A. Pedlar, ASP Conference Series 320, p. 142
- Weiss A., Walter F., & Scoville N. Z. 2005, *A&A*, 438, 533
- Weiss A., Downes D., Walter F., & Henkel C. 2007, in *From Z-Machines to ALMA: (Sub)Millimeter Spectroscopy of Galaxies* ASP Conference Series, Vol. 375, p.25
- Weiss A., Downes D., Neri R., Walter F., Henkel C., Wilner D. J., Wagg J., & Wiklind T. 2007, *A&A*, 467, 955
- White G. J., Ellison B., Claude S., Dent W. R. F., Matheson D. N. 1994, *A&A*, 284, L23
- Wilson C. D., Petitpas G. R., Iono D. et al. 2008, *ApJS*, 178, 189
- Wu J., Evans N. J. II., Gao Yu., Solomon P. M., Shirley Y. L., & Vanden Bout P. A. 2005, 635, L173
- Yao L., Seaquist E. R., Kuno N., & Dunne L. 2003, *ApJ*, 588, 771
- Young J. S. & Scoville N. Z. 1991, *ARA&A*, 29, 581
- Young J. S., Xie S., Tacconi L. et al. 1995, *ApJS*, 98 219
- Zenner S., & Lenzen R. 1993, *A&AS*, 101, 363
- Zhu M., Seaquist E. R., Kuno N. 2003, *ApJ*, 588, 243
- Zhu M., Papadopoulos P. P., Xilouris E. M., Kuno N., & Lisenfeld U. 2009, *ApJ*, 706, 941

This paper has been typeset from a $\text{\TeX}/\text{\LaTeX}$ file prepared by the author.